Reduced-Order Modeling of MEMS Using Modal Basis Functions

by

Mathew Varghese

B.S., University of California, Berkeley (1994)
S.M., Massachusetts Institute of Technology (1998)

Submitted to the Department of Electrical Engineering and Computer Science
in partial fulfillment of the requirements for the degree of

Doctor of Philosophy

at the

Massachusetts Institute of Technology

October 2001

Author _____
Department of Electrical Engineering and Computer Science
October 31, 2001

Certified by _____
Stephen D. Senturia
Barton L. Weller Professor of Electrical Engineering and Computer Science
Thesis Supervisor

Accepted by _____
Arthur C. Smith
Chairman, Department Committee on Graduate Students

Reduced-Order Modeling of MEMS Using Modal Basis Functions

By

Mathew Varghese

Submitted to the Department of Electrical Engineering and Computer Science
in October, 2001 in partial fulfillment of the requirements
for the Degree of Doctor of Philosophy

ABSTRACT

The field of MEMS has matured significantly over the last two decades increasing in both complexity and level of integration. To keep up with the demands placed by these changes requires the development of computer-aided design and modeling tools (CAD/CAM) that enable designers to reduce the time and cost it takes to produce working prototypes. An ideal scenario is one in which a designer is able to quickly model and simulate an entire microsystem – sensors, actuators and electronics -- with the certainty that their results will match that of physical prototypes. This vision of design requires the existence of system level models of MEMS devices that can capture the complex non-linear coupling between multiple physical domains, yet be sufficiently fast and compact in form to insert into a system dynamics simulator. In this thesis I explore techniques of automatically constructing such models from meshed representations of device geometry.

These dynamical models are known as "reduced-order" models or "macromodels." They are characterized by few degrees of freedom (DOF), and a small set of state equations. Our process for constructing macromodels is built upon two well-established methodologies – normal mode superposition and Lagrangian mechanics. This is referred to as the "CHURN process" and was originally developed by Gabbay et al. to create models of electromechanical devices with two electrodes under conditions satisfying linear mechanics. In this thesis I significantly extend this process to model multi-port magnetostatic devices, multi-port electrostatic devices, and geometrically non-linear mechanical devices exhibiting stress stiffening. I also address one of the key concerns in building macromodels -- the required degree of sophistication, and the extent of involvement, of a designer in the model construction process. I propose and implement several heuristic techniques that automate the model generation process. I also apply these techniques to a fabricated microelectromechanical high frequency filter and present verification of our modeling results.

Thesis Supervisor: Stephen D. Senturia
Barton L. Weller Professor of Electrical Engineering and Computer Science

To my mother and father,

for all their love

Acknowledgements

I take this opportunity to thank the many individuals that contributed to the completion of this thesis through their technical, financial and moral support.

First and foremost, I thank my advisor Steve Senturia for effectively guiding me through this thesis. He has always given me ample space to be creative and explore ideas that satisfy my intellectual curiosity while still keeping me on track. He has helped me significantly in identifying key problems to work on, and in addition, placing my work into context. He is primarily responsible for guiding my academic development over the last six years.

I want to thank Professor Jacob White for his support and key discussions that had significant impact on my research. I also wish to thank Professor Jeff Lang for his detailed review of my work and contributions as my thesis reader.

Coventor deserves thanks for their support of my work. I spent several productive summers developing reduced-order modeling tools within their MEMCAD framework. I specifically thank Vladimir Rabinovich for his generous help in getting me up to speed at Coventor and patience in answering all my questions. Vladimir has also significantly contributed to my research thorough many insightful discussions. I also thank John Gilbert for his effort in placing my work in a practical context by suggesting real world problems to tackle.

Past group members have been of great help in developing this thesis. Lynn Gabbay deserves special mention for providing the basis of this thesis through his development of the CHURN process. I also thank G. K. Ananthasuresh, Raj Gupta, Elmer Hung, Jan Mehner, Bart Romanowicz, Dan Sobek, V.T. Srikar, and Joseph Yang for the many stimulating conversations we have shared that have made it a pleasure to be at MIT and that have contributed in direct or indirect ways to my thesis. I thank Sharlene Blake for making my life easier dealing with administrative issues, Kurt Broderick for help in the

TRL (technology research laboratory) and the systems administration staff for help with maintaining our computers.

I want to thank Professor Mark Allen for giving me the opportunity to learn about fabrication and magnetic MEMS devices during my semester at Georgia Tech. I appreciate the time Jin Woo Park spent bringing me up to speed with fabrication processes. Jae Park also built several devices on my behalf. I thank all of my friends at Georgia Tech. for the many enjoyable discussions, and the wonderful time I had in Atlanta.

I thank my brother, Zubin, for his support over the years. He has always expressed a biased faith in my abilities from which I've derived great confidence. I also thank him for his review of my thesis and his numerous helpful comments.

My wife, Sharon, deserves special credit. She has been a great stabilizing influence on my life and been extremely supportive throughout my time at MIT.

My parents, to whom I dedicate this thesis, deserve significant credit for all my accomplishments. Their love and many sacrifices don't go unnoticed.

Support for this research was provided in part by the Defense Advanced Research Projects Agency under contract F30602-97-2-0333 and Coventor, Inc.

Contents

1 Introduction

The field of MEMS has matured significantly over the last two decades increasing in both complexity and level of integration [1][2][3]. MEMS development has also moved out of university and government research facilities into the laboratories of companies attempting to commercialize microfabrication technologies [4][5][6]. To keep up with the demands placed by these changes requires the development of computer-aided design and modeling tools (CAD/CAM) that enable designers to reduce the time and cost it takes to produce working prototypes [17]. An ideal scenario is one in which a designer is able to quickly model and simulate an entire microsystem – sensors, actuators and electronics -- with the certainty that their results will match that of physical prototypes. Verification of ideas and optimization of designs could then be done on inexpensive, but powerful, computer workstations instead of iterating through the slow and expensive task of fabricating test devices. This vision of design requires the existence of system level models of MEMS devices that can capture the complex non-linear coupling between multiple physical domains, yet be sufficiently fast and compact in form to insert into a system dynamics simulator [7][8]. In this thesis we explore techniques of automatically constructing such models from meshed representations of device geometry.

These dynamical models are known as "reduced-order" models or "macromodels." They are characterized by few degrees of freedom (DOF), and a small set of coupled ordinary differential equations (ODEs) as state equations. They are also accurate to full three-dimensional meshed simulations. Our process for constructing macromodels is built upon two well-established methodologies – normal mode superposition [16] and Lagrangian mechanics [9]. A significantly truncated set of normal modes (eigenvectors of the linear mechanical equations of motion) is used to express the positional state of a device and thus reduce the DOF. Differentiable and analytical representations for the kinetic and potential energies of the system in these truncated modal coordinates are then computed and used in Lagrangian equations of motion. These form the macromodel state equations. They capture the coupling between the various physical domains of the device

by describing the energy flow between these domains. Although the resulting state equations are fast to integrate in a system simulator, the model generation process requires the computationally expensive task of performing several single energy domain meshed simulations to create the analytical energy representations. This is a one-time cost incurred when a model is created that must be balanced against the benefits of a compact and fast macromodel.

This above process, referred to as the "CHURN process", was originally developed by Gabbay et al. [18] to create models of electromechanical devices with two electrodes under conditions satisfying linear mechanics. In this thesis we significantly extend this process to model multi-port magnetostatic devices, multi-port electrostatic devices, and geometrically non-linear mechanical devices exhibiting stress stiffening.

One of the key concerns in building macromodels is the required degree of sophistication, and the extent of involvement, of a designer in the model construction process. An automated means of macromodel creation is highly desirable. We propose and implement several heuristic techniques that minimize the degree of designer interaction in the model generation process. We also apply these techniques to a fabricated microelectromechanical high frequency filter and present experimental verification of our modeling results.

This thesis is organized into six chapters, one reference section, and two appendices. Chapter 2 introduces Gabbay's CHURN process and presents the prerequisite background for the remaining chapters. Chapter 3 explains how we extend CHURN to model multi-port magnetostatic devices. Chapter 4 explains why CHURN fails to capture the geometric mechanical non-linearity of stress stiffening, and proposes an alternative modeling scheme for creating an accurate macromodel. Chapter 5 details several heuristic techniques for automating the macromodeling process, and presents simulation and experimental results for a microelectromechanical high frequency filter. The conclusions of this thesis are then presented in Chapter 6.

1.1 Background

There are numerous techniques for constructing reduced-order models, or macromodels for MEMS, and it is our intent in the following sections to briefly introduce these techniques to place the work in this thesis into context. For a more comprehensive look at reduced-order models, we refer the reader to the review in [42].

There have always existed semi-analytical, ad hoc, models of MEMS devices [45][46][3]. State equations for these models are typically hand derived by a designer who has an intimate understanding of the physics of a particular device. However, there have recently emerged several approaches for the systematic, computer-aided, construction of reduced-order models that require less sophistication and involvement on the designer's part. They generally fall into two categories -- lumped element approaches and basis function approaches.

1.2 Lumped element approaches

There is a large class of MEMS devices that can be decomposed into a set of interconnected functional elements such as masses, springs, dampers, and capacitors. These elements are typically spatially discrete and easily identified from layout descriptions of devices (see Figure 1). Models for each functional element of a device are put together at the system level to form a complete macromodel description. These elements are often referred to as "lumped-elements" and can be modeled directly in the appropriate physical domain [49] or by using equivalent circuit elements [47]. This approach has the advantage that once parametric models exist for the various elements, putting these together at the system level to make highly complicated devices becomes relatively quick and straightforward. This type of modeling is particularly useful when a fabrication process is well defined and design variations are constrained to changes in device layout. A designer is also able to derive an intuitive understanding of a device's functionality directly from the system level schematic description of the interconnected device – analogous to a circuit designer deriving meaning from a circuit schematic. The disadvantage with this lumped-element approach, however, is that it is difficult to model the numerous devices that cannot easily be decomposed into functional components. In addition, modifications to device geometry other than those due to layout can require significant overhead, as models of the lumped elements must be re-derived every time.

1.3 Basis function approaches

Basis function approaches to macromodeling begin with the large set of nonlinear state equations of a meshed representation of a MEMS device, and use numerical techniques to reduce the model order. Our modal basis function approach falls under this category. A general form of the system's state equations may be written as follows [41]:

$$\frac{d\vec{y}(t)}{dt} = f(\vec{y}(t), \vec{u}(t)) \tag{1}$$

where $\vec{y}(t)$ is a vector of states of length N (often greater than a thousand), $f(\vec{y}(t), \vec{u}(t))$ is a non-linear vector-valued function, and $\vec{u}(t)$ is an input vector of length p. The system's states $\vec{y}$ are not necessarily the desired form for the output of the system, so an additional transformation may be required to compute the output.

Even though the system has a large set of states, an appropriate reduced set of states may be able to capture the system dynamics with negligible loss of accuracy. Consider the following projection onto a reduced state space:

$$\vec{y}(t) = \sum_{i=1}^{m} q_i(t)\vec{V}_i = [V]\vec{q}(t) \tag{2}$$

where $q_i(t)$ is the i^{th} state variable, $\vec{q}(t)$ is the reduced state vector of size m, expected to be much smaller than N. $\vec{V}_i$ is a basis vector, and $[V]$ is a matrix of these basis vectors which we select to be orthonormal. We use this projection to transform equation (1) to a reduced set of m state equations:

$$V^T \frac{d\vec{y}(t)}{dt} = \frac{d\vec{q}(t)}{dt} = V^T f(\vec{y}(t), \vec{u}(t)) \tag{3}$$

These equations may be used to calculate $\vec{q}(t)$, and therefore through equation (2) $\vec{y}(t)$. The success of the above technique is obviously dependent on the choice of the basis vectors $\vec{V}_i$. There are several methods of calculating a useful basis, including utilizing Krylov subspaces [11], singular value decomposition of state trajectories [12], and

neural-network principle component analysis [43]. In this thesis, we happen to use linear modal analysis [20] to compute a basis set.

Even though the number of state equations is reduced, the nonlinear function $f(\bar{y}(t))$ is still costly to compute. Efficient techniques for computing this term are required to make a macromodel truly compact and fast. Recently, several approaches have been proposed based on Taylor expansions [11] and piece-wise linear approximations about a trajectory [41]. In this thesis, we use a fast analytical representation of the force derived from a series of quasi-static meshed simulations [13][14][15].

Basis function techniques have the advantage that they can be applied to a large class of MEMS problems and are not typically restricted in geometry. The models, however, are most often "black-box" in nature, as designers have no intuitive feel for the basis functions used to reduce the order of a model. We suggest that modal basis functions might bridge this issue because many designers have prior experience with modal analysis, and even design devices with mode shapes in mind[2][3][21][22].

1.4 Network (system) representation

Regardless of how a macromodel is constructed, at the system level, it is represented as a network element that interacts with other network elements via electrical and mechanical "ports." A schematic description of a microelectromechanical band-pass test circuit is illustrated in Figure 2. It shows how various electronic, electromechanical, and mechanical components (macromodels) can be interconnected to form a complete description of a system. Components interact through "ports" that are defined by pairs of variables whose product is either energy or power. Electrical ports have either charge and voltage or current and voltage as through and across variables respectively. Mechanical ports have either force and amplitude or force and velocity as through and across variables respectively. The system simulator calculates dynamics by integrating component state equations while ensuring that shared across variables (voltage, displacement, or velocity) are consistent throughout the system and through variables (force, charge, or current) are conserved external to the components. The underlying state equations for the macromodels must be compact and fast to integrate because a simulator often has to handle a large number of components.

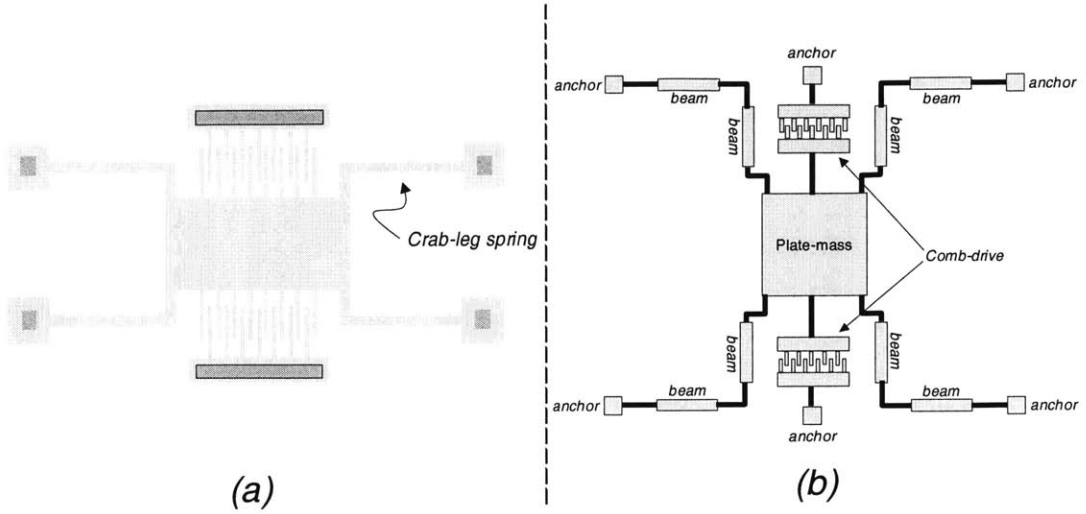

Figure 1 Crab-leg accelerometer [10]. (a) Simplified layout view. (b) Lumped-element model.

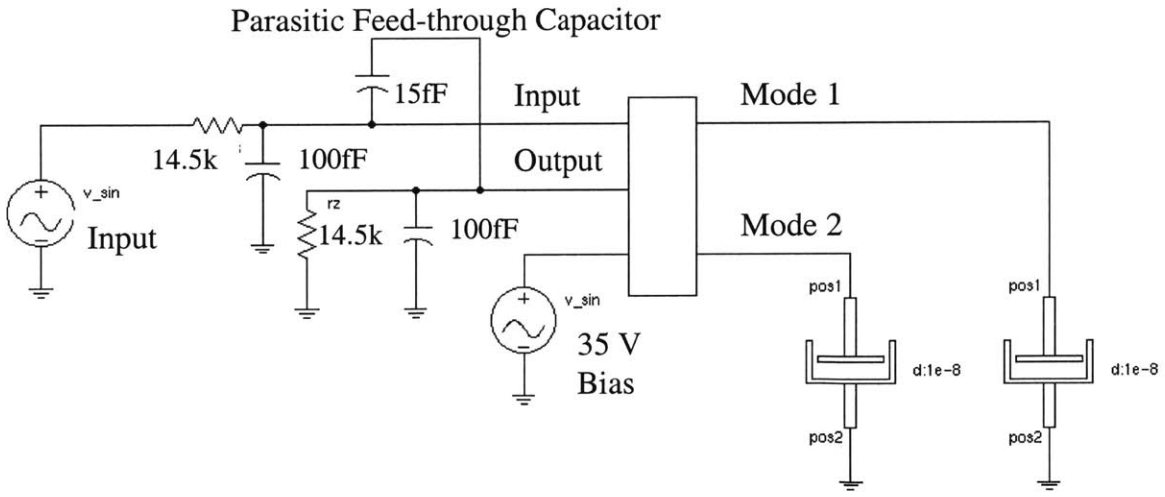

Figure 2 Test circuit for a microelectromechanical high-frequency filter [3].

2 The CHURN process

This chapter introduces the CHURN process [18] for constructing modal basis function based macromodels from meshed device representations. The work in this thesis extends CHURN in several different directions, so the theory behind the basic modeling process is a prerequisite for discussing our new contributions.

We begin with a brief definition of the meshes that are used to represent device geometry in this thesis. We then introduce the linear mechanical normal modes that are the basis functions in our modeling approach and also present some of the useful properties of these modes. The next two sections explain how normal modes can reduce the order of a model through a superposition of a truncated set of modes. Following this we show how the Lagrangian may be used to derive equations of motion in "modal coordinates".

2.1 Meshes

The finite element method (FEM) and boundary element method (BEM) solvers we use in this thesis perform simulations on discretized representations of device geometry known as "meshes." These meshes take many forms, but for the purposes of this thesis they are described by the positions of their nodes, with each node having three translational degrees of freedom (DOF). Thus, a mesh having N/3 nodes, has N DOF that must be specified to define its position. Mathematically, the DOF are specified in a single vector, $\vec{y}$, of length N, that will herein be called the "position vector."

2.2 Linear mechanical normal modes

The normal modes that are used throughout this thesis are the eigenvectors of the linear mechanical equation of motion (this is a linearized and Fourier transformed version of equation (1) under zero input conditions):

$$(4) \qquad \left(-\omega^2[M]_{NxN} + [K]_{NxN}\right)\vec{y} = 0$$

where ω is the frequency, $[M]_{NxN}$, is the mass matrix, and $[K]_{NxN}$ is the stiffness matrix associated with the mesh. A mode shape, $\vec{\varphi}_i$, specifies each eigenvector, along with a frequency eigenvalue, ω_i. $\vec{\varphi}_i$ is the positional state of the mesh in a particular mode shape. Each mode also has a scalar "modal mass," m_i, and "modal stiffness," k_i. In practice, when the modes are computed based on a mesh, an additional shape vector, $\vec{y}_{eqm}$, is also generated. This represents the shape of the mesh after it is allowed to relax due to any internal stresses. The mode shapes are then calculated about this relaxed mesh.

The normal modes (non-degenerate) are orthogonal over both the mass and stiffness matrices:

$$\vec{\varphi}_j^T [M]_{NxN} \vec{\varphi}_i = \delta_{ij} m_i \tag{5}$$

$$\vec{\varphi}_j^T [K]_{NxN} \vec{\varphi}_i = \delta_{ij} k_i \tag{6}$$

where δ_{ij} is the kronecker delta function ($\delta_{ij} = 1$ for $i = j$, and $\delta_{ij} = 0$ for $i \neq j$).

We define here the "modal matrix", $[P]_{NxN}$, that consists of column vectors of the mode shapes.

$$[P]_{NxN} = [\vec{\varphi}_1 \cdots \vec{\varphi}_N] \tag{7}$$

We also define the generalized mass matrix, $[m_G]_{NxN}$, and the generalized stiffness matrix, $[k_G]_{NxN}$.

$$[m_G]_{NxN} = [P]_{NxN}^T [M]_{NxN} [P]_{nxN} \tag{8}$$

$$[k_G]_{NxN} = [P]_{NxN}^T [K]_{NxN} [P]_{nxN} \tag{9}$$

These two matrices are diagonal because of the orthogonality conditions in equations (5) and (6). The diagonal entries are the modal mass and modal stiffness of the modes.

2.3 Modal co-ordinates

Given the mode shapes, another equivalent mathematical means of specifying the position of the mesh is to use a superposition of the linear mechanical normal modes according to:

$$\vec{y} = \vec{y}_{eqm} + \sum_{i=1}^{N} q_i \vec{\varphi}_i = \vec{y}_{eqm} + [P]_{NxN} \vec{q}_{Nx1} \tag{10}$$

where $\vec{y}_{eqm}$ is the equilibrium position of the mesh after relaxation due to any internal stresses, q_i are scalar, non-dimensional mode amplitudes, $\vec{q}^{Nx1}$ is a vector of length N specifying all the mode amplitudes, $\vec{\varphi}_i$ is the mechanical "mode shape", and $[P]^{NxN}$ is the "modal matrix" consisting of column vectors of the mode shapes. The mesh position is uniquely defined by either specifying the vector, $\vec{y}$, or equivalently, specifying the vector, $\vec{q}^{Nx1}$. Thus, $\vec{q}^{Nx1}$ provides an alternative "modal co-ordinate" system for the mesh position.

At this point it is important to point out that although the mode shapes were calculated from a linear mechanical analysis, it is perfectly valid to continue using modal superposition to specify the position of the mesh when the mechanical system becomes non-linear. The vector $\vec{q}_{Nx1}$ acts purely as an alternative co-ordinate system to $\vec{y}$, and is independent of the underlying physics of the mesh.

2.4 Model order reduction

The modal co-ordinates are very useful because the sum in equation (10) does not need to include all N modes to accurately approximate the positional state of the mesh. In fact, only a small set of low order modes, *m*, typically less than five, is required. This method of truncating the sum, and hence reducing the DOF dramatically, is well established for analyzing dynamic mechanical systems [16].

$$\vec{y} \approx \vec{y}_{eqm} + \sum_{i=1}^{m} q_i \vec{\varphi}_i = \vec{y}_{eqm} + [P]_{Nxm} \vec{q}_{mx1} \tag{11}$$

$[P]_{Nxm}$ is the truncated modal matrix, and $\vec{q}_{mx1}$ is the truncated modal amplitude vector. For ease of notation, $[P]_{Nxm}$ will be written as $[P]$, and $\vec{q}_{mx1}$ will be written as $\vec{q}$, for the remainder of this thesis.

Anathasuresh [20] demonstrated that the higher order modes had negligible effect on the response of electromechanical systems and constructed models based on a reduced number of modes. He projected the equations of motion for an electrostatic system

$$[M]_{NxN}\,\ddot{\vec{y}} = \vec{F}^{Nx1}_{electrostatic}(\vec{y},\vec{u}) + \vec{F}^{Nx1}_{mechanical}(\vec{y}) \tag{12}$$

onto the truncated modal co-ordinates to reduce the number of equations of motion from N to m.

$$[P]^T[M]_{NxN}[P]\ddot{\vec{q}} = [P]^T\vec{F}^{Nx1}_{electrostatic}(\vec{y},\vec{u}) + [P]^T\vec{F}^{Nx1}_{mechanical}(\vec{y}) \tag{13}$$

$\vec{F}^{Nx1}_{electrostatic}(\vec{y},\vec{u})$ is the electrostatic force, and $\vec{F}^{Nx1}_{mechanical}(\vec{y})$ is the elastic response force on each mesh node. The inertial term on the left side of equation (13), reduces to $[m_G]_{mxm}\ddot{\vec{q}}$, where $[m_G]_{mxm}$ is the generalized modal mass matrix which is diagonal. The modes are therefore decoupled from each other in this inertial term. In addition, for the special case when the mechanics are linear, the mechanical forces, are also decoupled and given by:

$$[P]^T_{Nxm}\vec{F}^{Nx1}_{mechanical}(\vec{y}) = -[P]^T[K]_{NxN}\vec{y} = -[P]^T[K]_{NxN}[P]\vec{q} = -[k_G]_{mxm}\vec{q} \tag{14}$$

$[k_G]_{mxm}$ is the diagonal generalized modal stiffness matrix. The projection onto the modes, not only reduces the number of equations of motion, but also simplifies the inertial and stiffness terms, significantly speeding up the solution time for this model over one with the full DOF.

The disadvantage with the above model (equation (13)) is that it requires explicit computation, using a mesh, to calculate the electrostatic forces when the equations of motion are integrated in time. In addition, when the mechanics are non-linear, the mechanical forces also require an explicit computation on the mesh. This makes the

above model inappropriate for insertion into system level simulators that model the interaction of the electromechanical system with electronics. A compact, self-contained model that does not depend on meshed simulations during integration is required for these simulators.

Ideally, the mechanical and electrostatic forces should be expressed directly in modal co-ordinates, be fast to compute, and have a compact representation that is easily inserted into system simulators. An analytical representation of the forces would fit these criteria.

2.5 Lagrangian

The Lagrangian, $L(\vec{q},\dot{\vec{q}},t)$, is a powerful tool for modeling the coupling between conservative energy domains. It keeps track of the energy flowing between different energy domains in a system (kinetic, elastic, electrostatic, magnetic), and has the advantage that it is not tied to any particular co-ordinate system [40]. As we will show, the Lagrangian is a convenient means of deriving equations of motion for a system, and a path to obtaining compact, fast, analytical representations of non-linear forces.

$$L\left(\vec{q},\dot{\vec{q}},t\right)=T\left(\vec{q},\dot{\vec{q}},t\right)-U(\vec{q},\dot{\vec{q}},t) \tag{15}$$

$T\left(\vec{q},\dot{\vec{q}},t\right)$ and $U(\vec{q},\dot{\vec{q}},t)$ are the kinetic and potential energy of the system respectively. The Lagrangian is a scalar function of the generalized co-ordinates, $\vec{q}$, the generalized velocity, $\dot{\vec{q}}$, and the time, t. The m equations of motion of the reduced system are derived from Lagrange's equations:

$$\frac{d}{dt}\left(\frac{\partial L}{\partial \dot{q}_i}\right)-\frac{\partial L}{\partial q_i}=0 \tag{16}$$

These equations do not require a projection of forces into generalized co-ordinates, but do require knowledge of the system's kinetic and potential energies expressed in these co-ordinates. Although any generalized co-ordinates could be used with the Lagrangian, the use of modal co-ordinates, $\vec{q}$, enables several useful simplifications including the reduction of model order using a truncated modal superposition as we saw in section 2.4.

2.6 Kinetic energy, potential energy, and forces

The kinetic energy of the system has a simple analytical representation in modal co-ordinates

$$T(\vec{q},\dot{\vec{q}},t)=\sum_{i=1}^{m}\frac{1}{2}m_i\dot{q}_i^2 \tag{17}$$

where the "modal mass," m_i, is the i^{th} diagonal entry in the modal mass matrix, $[M_G]_{mxm}$.

In general, the potential energy, $U(\vec{q},\dot{\vec{q}},t)$, is the sum total of the energy domains in the system [28].

$$U(\vec{q},\dot{\vec{q}},t)=\sum_{\substack{\text{each energy}\\ \text{domain d}}}U_d(\vec{q},\dot{\vec{q}},t) \tag{18}$$

For an electromechanical system, the potential energy consists of elastic and electrostatic terms. In this case the Lagrangian equations of motion (16) reduce to

$$\frac{d}{dt}\left(\frac{\partial T}{\partial \dot{q}_i}\right)=-\frac{\partial U_{elastic}}{\partial q_i}-\frac{\partial U_{electrostatic}}{\partial q_i} \tag{19}$$

where $U_{elastic}$ and $U_{electrostatic}$ are independent of modal velocity and time. The term on the left is the inertial force, and the terms on the right are the elastic and electrostatic forces. As we saw previously, for compactness and computational efficiency, it is desirable to have an analytical representation of these forces. This is possible, if the kinetic and potential energies themselves are differentiable, analytical representations.

In the previous section, the kinetic energy was expressed in just such a form, so the inertial term can readily be calculated.

$$\frac{d}{dt}\left(\frac{\partial T}{\partial \dot{q}_i}\right)=m_i\ddot{q}_i \tag{20}$$

In addition, for the special case when the mechanics are linear, the elastic potential energy also has a simple analytical representation in modal co-ordinates

$$U_{\substack{\text{linear}\\ \text{elastic}}}\left(\bar{q},\dot{\bar{q}},t\right)=\sum_{i=1}^{m}\frac{1}{2}k_i\bar{q}_i^2 \tag{21}$$

where k_i, known as the "modal stiffness," is the i^{th} diagonal entry in the modal stiffness matrix, $[k_G]_{mxm}$ and is also equal to $m_i\omega_i^2$. Combining this elastic energy with the calculated inertial term, the equations of motion become:

$$m_i\ddot{q}_i=-k_iq_i-\frac{\partial U_{electrostatic}}{\partial q_i} \tag{22}$$

It remains, therefore, to find a differentiable analytical representation of the electrostatic potential energy to complete this model. If the mechanics were non-linear, equation (21) would not hold and the same would have to be done for the elastic potential energy as well. Gabbay [28] developed a methodology to compute just such analytical representations.

2.7 Analytical energy representations

Gabbay's "CHURN" methodology for computing differentiable analytical representations for the potential energy is based on fitting functions to a set of FEM or BEM simulations performed on a mesh. In Anthasuresh's methodology, meshed simulations are always required to compute forces. CHURN shifts the computational cost of performing meshed simulations to the one-time construction of a reduced-order model, after which forces are computed from fast, compact, analytical representations.

The CHURN methodology is depicted in Figure 3. A bounded region of mode space, which is the expected operating range of a system, is sampled in potential energy through a series of meshed simulations. These representative samples are then fitted to a multivariate polynomial to obtain a differentiable analytical representation of the potential energy valid within this operating space, with accuracy comparable to meshed simulations.

(23) $$U_d(q_1,\ldots,q_m)=\sum_{i_1=0}^{R_1}\cdots\sum_{i_m=0}^{R_m}a_{i_1\cdots i_m}q_1^{i_1}\cdots q_m^{i_m}$$

R_i is the order of mode q_i, and $a_{i_1\cdots i_m}$ is a fitting co-efficient of the polynomial. This methodology is not restricted to the use of polynomials – rational polynomials, or other types of functions can also be used. Details of the procedure for obtaining a representative sample, and performing a fit are given in [28].

2.8 Electrostatic co-energy

Although the methodology outlined above is intended to be quite general, its implementation is dependent on the particular energy domain in question. In the electrostatic case, it is the capacitance that is found as an analytical representation using CHURN and not the electrostatic energy directly. This energy and its partial derivative are then computed from the capacitance.

(24) $$U_{electrostatic}=\frac{1}{2}\frac{Q^2}{C(q_1,\cdots q_m)}$$

(25) $$\left.\frac{\partial U_{electrostatic}}{\partial q_i}\right|_{Q,\vec{q}}=\frac{1}{2}Q^2\frac{\partial}{\partial q_i}\left(\frac{1}{C(q_1,\cdots q_m)}\right)\Bigg|_{\vec{q}}$$

In practice, Gabbay chose to use the electrostatic co-energy [31] to model this domain for reasons of convenience. The co-energy, $U^*_{electrostatic}$, and its partial derivative are given by

(26) $$U^*_{electrostatic}=\frac{1}{2}V^2C(q_1,\cdots q_m)$$

(27) $$\left.\frac{\partial U^*_{electrostatic}}{\partial q_i}\right|_{V,\vec{q}}=\frac{1}{2}V^2\left.\frac{\partial C(q_1,\cdots q_m)}{\partial q_i}\right|_{\vec{q}}=-\left.\frac{\partial U_{electrostatic}}{\partial q_i}\right|_{Q,\vec{q}}$$

In the Lagrangian equations of motion, the partial derivative of the energy is replaced with the partial derivative of the co-energy including the change of sign.

(28) $$m_i\ddot{q}_i=-k_iq_i+\left.\frac{\partial U^*_{electrostatic}}{\partial q_i}\right|_{V,\vec{q}}$$

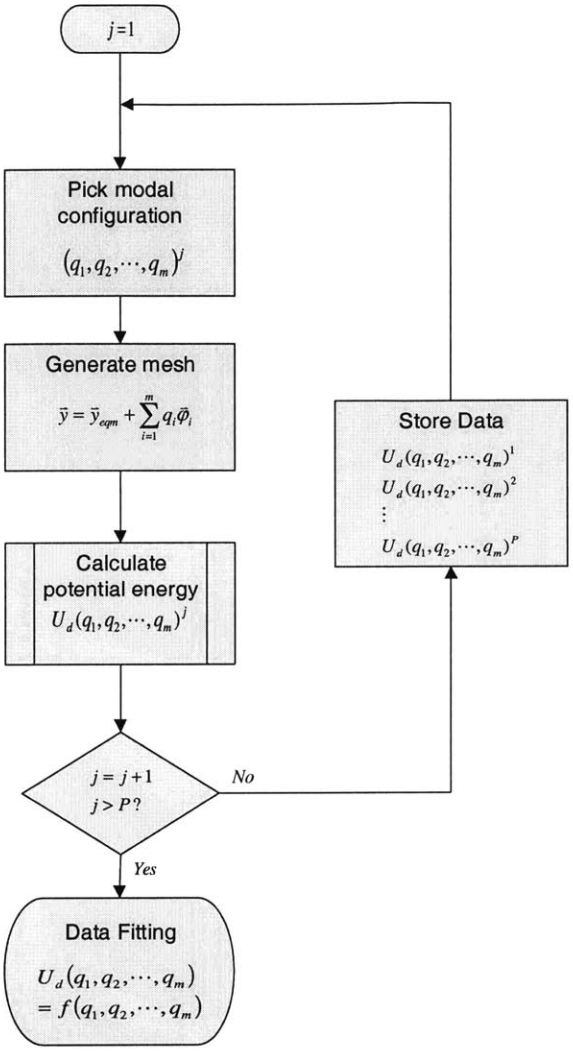

Figure 3 Generic CHURN methodology for creating differentiable analytical representations of potential energy.

2.9 CHURN macromodel construction

Gabby [28] implemented a systematic semi-automated process to create macromodels of electromechanical systems for insertion into system simulators. This implementation referred to as the "CHURN process," is outlined in Figure 4.

A designer begins by constructing a mesh for a device under study. This mesh typically has thousands of nodes, and hence, thousands of degrees of freedom. A truncated set of m modes are then selected, and normal mode superposition is used to reduce the order of the model without sacrificing accuracy as we saw in section 2.4. The procedure for selecting relevant modes is discussed in detail in [28]. It involves performing a full 3-D coupled simulation using the Co-Solve EM tool [29], and analyzing the results to determine which modes are most excited. A designer is ultimately responsible for selecting the relevant modes.

Based on this reduced set of modes, analytical representations are found for the kinetic energy, elastic strain (elastostatic) energy, and electrostatic co-energy. The energy functions for each domain are computed separately. Equation (17) is used to compute the kinetic energy. The CHURN methodology in section 2.7 computes an analytical representation (rational polynomial) for the capacitance, which is used in the electrostatic energy or co-energy. For systems approximated by linear mechanics, equation (21) is used to compute the elastostatic energy. For systems with non-linear mechanics, Gabbay proposed to use the CHURN methodology to compute polynomials representing strain energy. However, as we will see in Chapter 4, this approach was unsuccessful. Therefore, without any modification, Gabbay's CHURN process is restricted to model linear mechanical systems.

Finally, given analytical representations of the system energies, the equations describing the macromodel are derived (equations (29)). The first set of equations defines the capacitance, the charge, and the rate of charge flow in the system. The second set of equations is the Lagrangian equations of motion. The charge, mode amplitudes, and modal velocities form the system's state variables.

(29)
$$\begin{bmatrix} C(q_1,\cdots,q_m) = f_{rational\_polynomial}(q_1,\cdots,q_m) \\ Q_1 = C(q_1,\cdots,q_m)V_1 \\ I_1 = \dot{Q}_1 \end{bmatrix}$$
$$\begin{bmatrix} m_1\ddot{q}_1 = -k_1 q_1 + \frac{1}{2}V_1^2 \frac{\partial C(q_1,\cdots,q_m)}{\partial q_1} \\ \vdots \\ m_m\ddot{q}_m = -k_m q_m + \frac{1}{2}V_1^2 \frac{\partial C(q_1,\cdots,q_m)}{\partial q_m} \end{bmatrix}$$

These equations are implemented in the SABER/MAST [34] hardware description language that is a precursor to VHDL-AMS [35]. This is a language that enables the description and simulation of analog mixed signal (AMS) systems and includes the description of state equations encompassing multiple energy domains.

2.10 Extending CHURN

The CHURN process that we present in this chapter is applicable to any conservative physical domain. In the following chapter we show how this process is adapted for modeling magnetic MEMS devices.

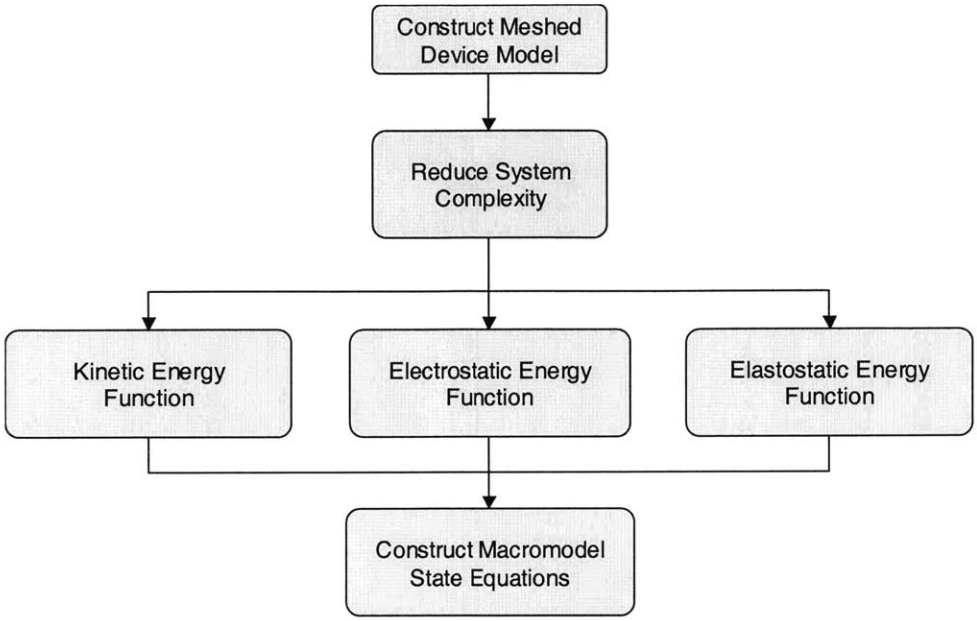

Figure 4 Overview of the "CHURN process" for constructing Macromodels of electromechanical systems.

3 Magnetics

There now exists a small but growing number of microactuators and microsensors that operate in the magnetic energy domain. Examples of these devices are magnetometers **[21]**, scanning mirrors [22], gyroscopes [23], flexural plate wave devices [24], and relays [25]. We perceive a need arising among designers of this group of devices for tools that make the task of modeling and design both easier and faster. The essential physics of these devices lies in the coupling between the magnetic and mechanical energy domains. There already exist commercial finite element tools that have the capability to model this interaction [27], but the designer often finds that the coupling must be handled manually, or through specifically written scripts. In addition, it is desirable to model the dynamics of a device, including any interaction with supporting electronic components. The task of performing a mechanically dynamic coupled simulation, required for system level modeling, is too slow with a FEM or BEM solver.

In this chapter we extend the CHURN process to create macromodels of magnetic devices. Our formulation, based on the magnetic co-energy, is applicable to model the Lorentz force (see Figure 5) and forces in devices with linear permeable materials. This chapter begins with an overview of the modeling strategy. The derivation of forces from the magnetic co-energy is then presented with an explanation of how an analytical representation of the co-energy is computed. Finally, we present results for a device used as an example of realistic Lorentz force devices that are actuated by external magnetic fields.

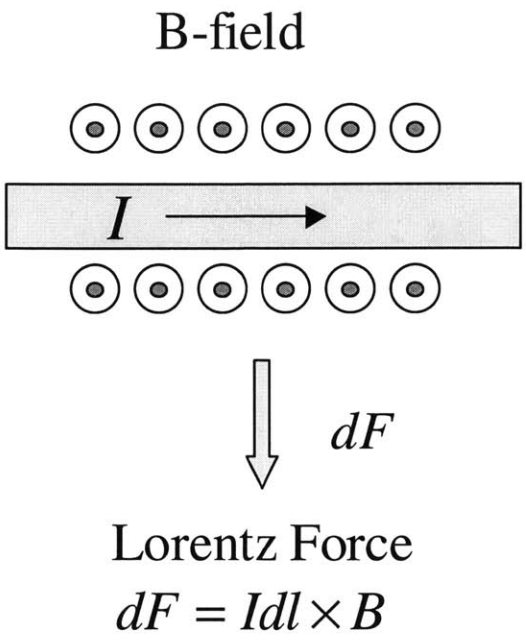

Figure 5 Lorentz force acting on a segment of current of length dl.

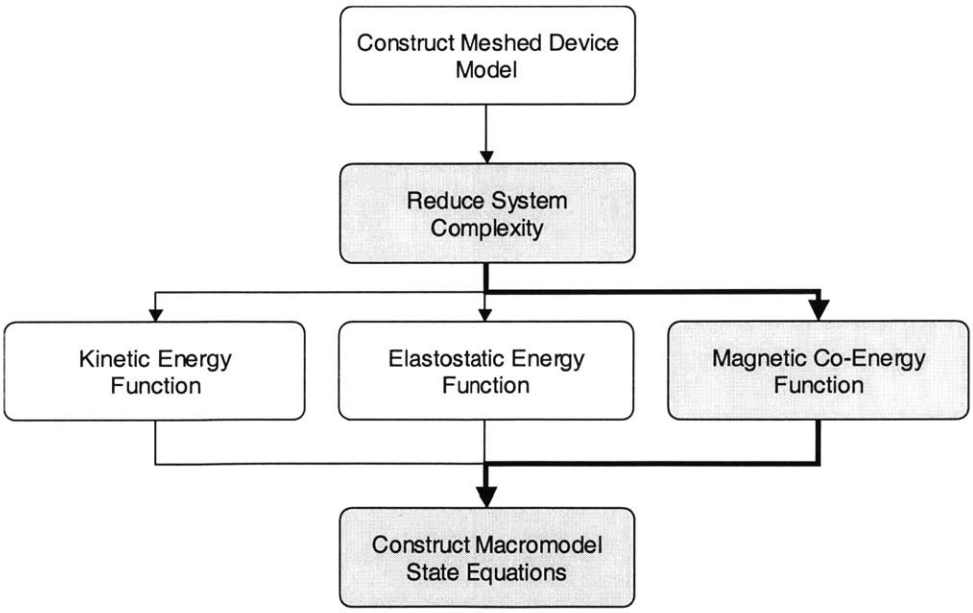

Figure 6 Methodology for macromodel construction for magnetic devices. The new contributions are shaded in gray.

3.1 Adapting the CHURN process

In Chapter 2 we saw how the CHURN process coupled the electrostatic and mechanical energy domains together in a reduced-order model through the Lagrangian. We propose a similar process to model magnetic forces, replacing the electrostatic co-energy with the magnetostatic co-energy, as shown in Figure 6. The Lagrangian equations of motion, for a reduced set of modal co-ordinates, form the basis of this macromodel's state equations:

$$m_i \ddot{q}_i = -k_i q_i + \left. \frac{\partial U^*_{magnetostatic}}{\partial q_i} \right|_{\vec{I},\vec{q}} \tag{30}$$

As with electrostatics, it remains, therefore, to find a differentiable analytical representation of the magnetostatic co-energy to complete this model

3.2 Magnetic co-energy

Before going further, it is instructive to derive the magnetic co-energy and how a magnetic "modal force" is calculated from this co-energy. Consider a device with two electrical ports, and modeled using just one mechanical mode, q_1. The network energy storage element in Figure 7 is a useful representation of this device in which each port is defined by pairs of variables whose product (energy) is conserved. The through and across variables for the electrical ports are current, i_j, and flux linkages, λ_j, respectively. The through and across variables for the mechanical port are modal force, f_1, and modal amplitude, q_1, respectively. The ports govern energy flow in and out of the device according to

$$\frac{dU_{magnetostatic}}{dt} = v_1 i_1 + v_2 i_2 + f_1 \frac{dq_1}{dt} \tag{31}$$

where $U_{magnetostatic}$ is the stored magnetic energy, v_j is the voltage across the electrical ports and is equal to the rate of change of flux linkages, $\frac{d\lambda_j}{dt}$.

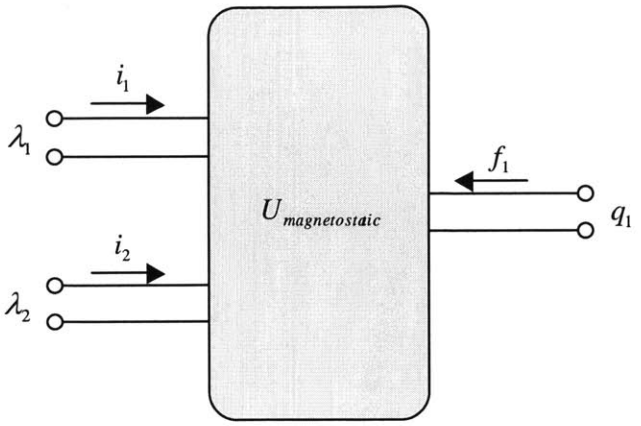

Figure 7 Network storage element representation of a conservative magnetic device with two electrical ports and modeled using just one mechanical mode (one mechanical port).

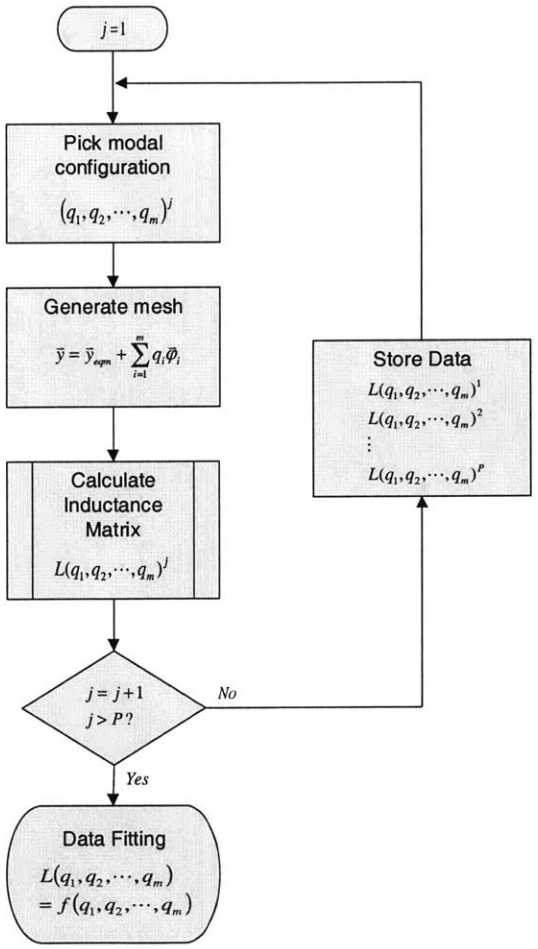

Figure 8 Overview of the process used to develop an analytical function representation of the inductance.

Multiplying through by dt, and substituting for the voltage we obtain

(32) $$dw_m = i_1 d\lambda_1 + i_2 d\lambda_2 + f_1 dq_1$$

We now define the magnetic co-energy as

(33) $$U^*_{magnetostatic} = (i_1\lambda_1 + i_2\lambda_2) - w_m$$

and use the following identity

(34) $$d(i_1\lambda_1 + i_2\lambda_2) = (\lambda_1 di_1 + \lambda_2 di_2) + (i_1 d\lambda_1 + i_2 d\lambda_2)$$

to recast equation (32) as

(35) $$dU^*_{magnetostatic} = \lambda_1 di_1 + \lambda_2 di_2 - f_1 dq_1$$

Now, the change $dU^*_{magnetostatic}$ is also given by

(36) $$dU^*_{magnetostatic} = \frac{\partial U^*_{magnetostatic}}{\partial i_1} + \frac{\partial U^*_{magnetostatic}}{\partial i_2} + \frac{\partial U^*_{magnetostatic}}{\partial q_1}$$

In order for equation (35) and equation (36) to be consistent, the flux linkages and force must equal:

(37) $$\lambda_1 = \left.\frac{\partial U^*_{magnetostatic}}{\partial i_1}\right|_{i_2,\bar{q}} \quad , \quad \lambda_2 = \left.\frac{\partial U^*_{magnetostatic}}{\partial i_2}\right|_{i_1,\bar{q}}$$

(38) $$f_1 = -\left.\frac{\partial U^*_{magnetostatic}}{\partial q_1}\right|_{i_1,i_2,\bar{q}}$$

Equation (38) is a convenient way to calculate the generalized force, f_1, if the magnetic co-energy is known. Thus, it remains to find the co-energy. One means of doing this is by integrating equation (35)

(39) $$U^*_{magnetostatic} = \int (\lambda_1 di_1 + \lambda_2 di_2 - f_1 dq_1)$$

Since the system is conservative, the co-energy is independent of the integration path. Therefore, consider integrating the terms $f_1 dq_1$ first, with all currents in the system set to zero. The force f_1 *is* zero in the absence of currents and fields from permanent magnets, so the contribution of the integral $\int f_1 dq_1$ is also zero.

The next step is to integrate the terms $\lambda_1 di_1$, and $\lambda_2 di_2$. To perform this integral it is convenient to express the flux linkages λ_i in terms of the currents i_i using the inductance matrix $[L]$ associated with the system

$$\begin{bmatrix} \lambda_1 \\ \lambda_2 \end{bmatrix} = \begin{bmatrix} L_{11} & L_{12} \\ L_{21} & L_{22} \end{bmatrix} \begin{bmatrix} i_1 \\ i_2 \end{bmatrix} \tag{40}$$

Each of the inductance entries is a function of the positional state, q_1. Keeping in mind that equation (39) is a path integral, the magnetic co-energy now evaluates to

$$U^*_{magnetostatic} = \frac{1}{2} L_{11}(q_1) i_1^2 + L_{12}(q_1) i_1 i_2 + \frac{1}{2} L_{22}(q_1) i_2^2 \tag{41}$$

One possible path is to move along each current "axis" sequentially, increasing i_1 to its final value, then i_2. Using this form of the co-energy, the force f_1 in equation (38) becomes

$$f_1 = -\frac{1}{2} \frac{\partial L_{11}(q_1)}{\partial q_1} i_1^2 - \frac{\partial L_{12}(q_1)}{\partial q_1} i_1 i_2 - \frac{1}{2} \frac{\partial L_{22}(q_1)}{\partial q_1} i_2^2 \tag{42}$$

The problem of finding an analytical representation for the force f_1 therefore reduces to finding an analytical form for the inductance L_{ij}.

3.3 Model construction

The task of finding an analytical function for the inductance is exactly analogous to finding an analytical function for capacitance in the CHURN methodology. The general procedure for obtaining the inductance function is shown in Figure 8. This function is

obtained by fitting data from a set of full 3-D meshed simulations. The simulations are performed using a FEM/BEM tool, which calculates the n-port inductance matrix, associated with a given mesh. Our implementation uses MemHenry [29], a tool dedicated to inductance calculations for conducting loops of "wire", in the absence of any magnetic material. For devices containing linear permeable materials, an alternative solver such as AMPERES [26] may be used for calculating inductance matrices. The simulations are repeated for a set of different positional states to generate data for a fitting algorithm. The next step is to fit each entry in the inductance matrix, using the generated data, to an analytical representation. In keeping with the original CHURN process, a multivariate rational polynomial was selected, although it is possible to use polynomials and other types of functions.

$$L_{lm} = \frac{\sum_{i_1=0}^{R_1}\sum_{i_2=0}^{R_2}\cdots\sum_{i_m=0}^{R_m} a_{i_1 i_2 \ldots i_m} q_1^{i_1} q_2^{i_2} \ldots q_m^{i_m}}{\sum_{i_1=0}^{S_1}\sum_{i_2=0}^{S_2}\cdots\sum_{i_m=0}^{S_m} b_{i_1 i_2 \ldots i_m} q_1^{i_1} q_2^{i_2} \ldots q_m^{i_m}} \tag{43}$$

L_{lm} is the inductance seen between ports l and m. a and b are fitting coefficients. The resulting analytical inductance functions are as accurate as the 3-D meshed simulations from which they were derived.

The next step is to construct an analytical representation of the magnetic co-energy function in equation (41) using the inductances L_{lm}. Since the inductance functions are rational polynomials, it is possible to take the analytic partial derivative of the co-energy and hence obtain the forces f_i given in equation (42).

3.4 Results

The methodology described in the previous sections is demonstrated using a device representative of typical Lorentz force actuated MEMS. The Lorentz force is generated when a current flows in a direction perpendicular to a magnetic field. Figure 5 shows the force, dF, acting on a small straight segment of current of length dl, exposed to a magnetic flux density B. The Lorentz force on this small segment is the cross product

$Idl \times B$. The device, depicted in Figure 9, is an elastic beam forming one side of a square, conducting loop. The device is placed in a homogenous z-directed magnetic field. The beam experiences a Lorentz force along its length and deforms. Since our methodology is based on representing a magnetic system using an inductance matrix, it is not possible to readily insert the boundary condition of a z-directed magnetic field without modifying the formulation.

To circumvent this problem, we surround the device with a cylindrical shell that creates a z-directed field. The magnetic field inside a long cylindrical shell is given by:

$$H_z = K_\phi \tag{44}$$

The system is now, electrically, a two-port element with port one belonging to the square loop, and port two belonging to the shell. The current entering the shell controls the magnetic field.

With this in place, the next step is to construct the macro-model. We simplify this example for clarity by using only the fundamental mode (q_1) and the first harmonic mode (q_2) of the elastic beam. For small deflections we expect only the fundamental mode to be excited.

Figure 10 shows the fitted inductance L_{12} as a function of the fundamental mode amplitude. Figure 11 shows the static deflection (y direction) of the beam for varying external magnetic fields. Our results compare well with those of a finite difference model of the beam in a magnetic field.

Figure 12 shows the deflection of the beam (y direction) as a function of the primary current with no external magnetic field. This is due to a "self-force" and acts to enlarge the current loop. This effect is negligible for typical Lorentz force devices because the current densities necessary for actuation are impractical. However, this "self-force" is significant in devices with magnetically permeable material, and our demonstration indicates that our methodology might be applicable to this class of devices.

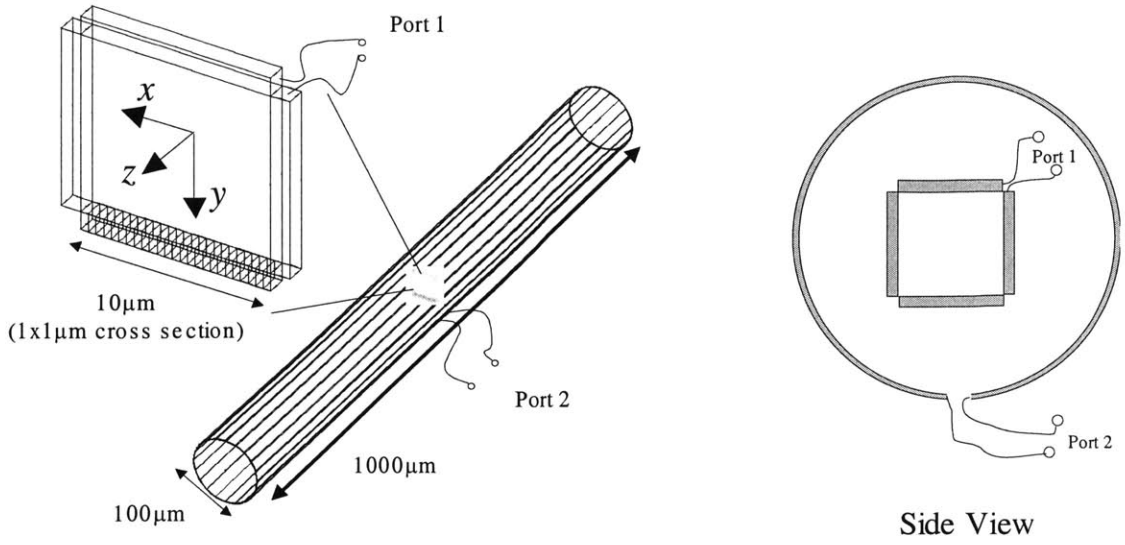

Figure 9 This is an example of a Lorentz force device. The elastic beam, shown as the bottom segment of the conducting loop, has a Young's Modulus of 130Gpa. The cylindrical shell has a slot cut out of it to form port 2 and generates an axial magnetic field (z-direction). Current I_1 flows into port1 and I_2 flows into port 2.

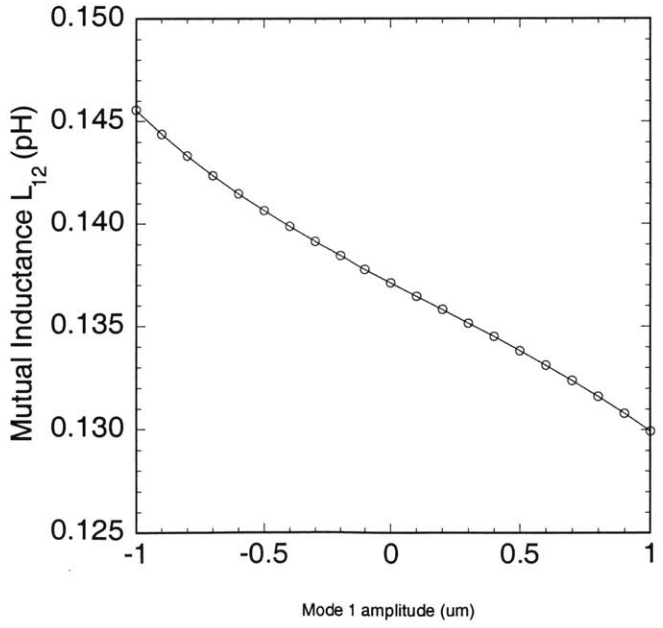

Figure 10 Mutual inductance, L_{12}, as a function of the fundamental mode amplitude.

As with the CHURN methodology, once the initial effort is made to construct the macro-model, further analysis is very fast. Static analysis, such as a the deformation shown in Figure 11, takes only a few seconds to perform in MATLAB while retaining high accuracy. Dynamics simulations are also very fast, as force calculations require only a function call to the analytic force representations.

3.5 Non-linear permeable materials

Modeling other types of magnetic devices is a natural extension of the work we have presented in this chapter. The co-energy formulation is still applicable to devices that have non-linear permeable materials as long as the magnetic energy domain is still conservative (no hysteresis). The most common material non-linearity is the saturation of magnetic flux. If the magnetic system is described in terms of an inductance matrix, saturation leads to a current dependence of the inductance that is not captured by our polynomial representation. Thus, although a co-energy formulation is still valid, we must modify the CHURN process to create an alternative representation that captures the current dependence accurately.

3.6 Summary

This chapter discusses the extension of the CHURN process to the magnetic energy domain. The magnetic co-energy is derived based on the inductance matrix and the CHURN methodology is modified to compute analytical representations of the self- and mutual- inductances.

A cylindrical shell simulating an externally applied magnetic field is introduced to model practical Lorentz force devices within the magnetic co-energy formulation. Results based on an example representative device are also presented.

In the future, it may be possible to extend the magnetic co-energy formulation further to model non-linear permeable material devices as long as the current dependence of inductance is taken into account.

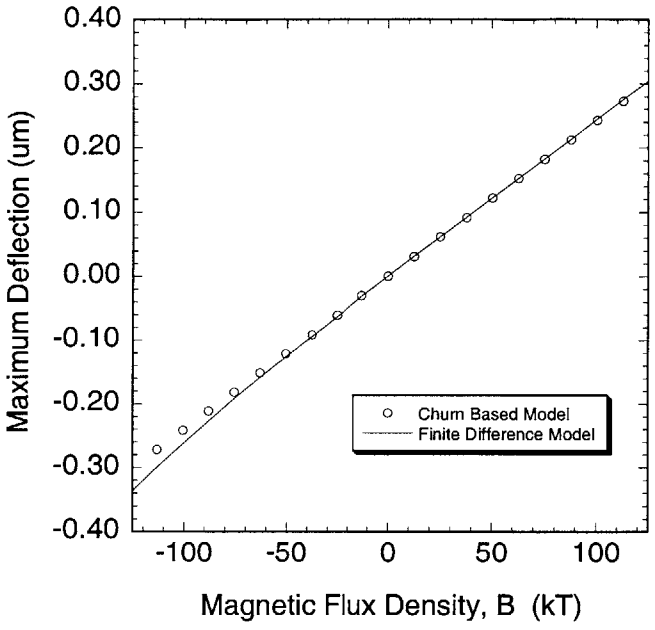

Figure 11 Maximum deflection of the elastic beam as a function of the axial magnetic flux density. The large magnetic field required for actuation is due to the high stiffness of the short beam. Practical devices are typically actuated in fields below 1T.

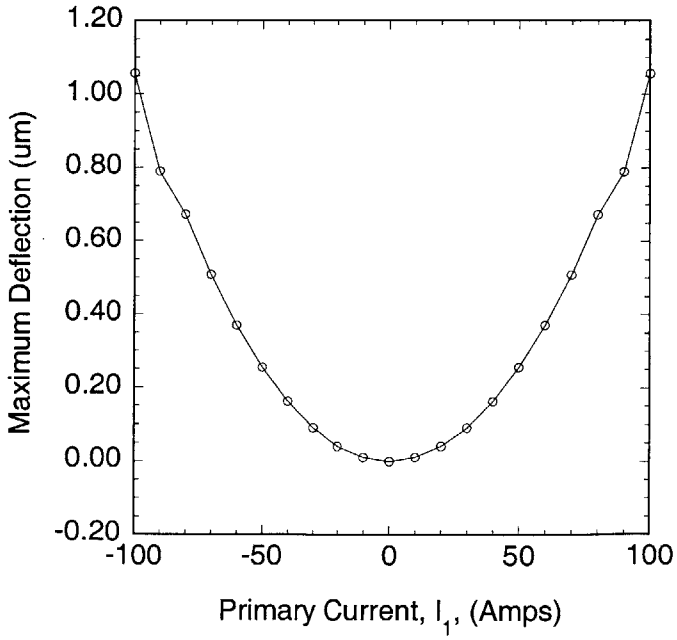

Figure 12 Maximum deflection of the elastic beam as a function of the loop current I_1, with no external field. The beam bends to increase the area of the loop independent of the direction of the current. The current required to achieve this actuation is excessively large. This "self-force" is not used to actuate real Lorentz force devices.

4 Stress stiffened mechanics

The macro-models presented in the previous chapters have all assumed, for simplicity, that the mechanical forces are linear in mode amplitude. Only the electrostatic and magnetostatic forces were modeled as non-linear using the CHURN process. There are, however, many devices that exhibit non-linear mechanical forces [38], particularly when the amplitude of motion is on the order of a structure's cross-sectional dimensions. Gabbay [28] attempted to extend the CHURN process to encompass non-linear mechanics, but he found that his models were inaccurate.

In this chapter we focus on one particular type of mechanical non-linearity, referred to as stress stiffening, that is common in MEMS devices. We begin by explaining the cause of this non-linearity, and then examine why the CHURN process fails to capture its effects accurately. Mehner's [19] modification of the CHURN process to capture stress stiffening, for a restricted class of devices, is then presented as a prelude to our more general approach using modal forces. We present the algorithm for our "modal-force" methodology and also a justification for its success. In addition, we present in Appendix C a detailed derivation, based on singular perturbation methods [30][50], that explains CHURN's failure and our "modal-force" methodology's success. We conclude this chapter with a presentation of our results for a clamped-clamped beam example and also for an asymmetrically supported plate actuated by an off-center electrode.

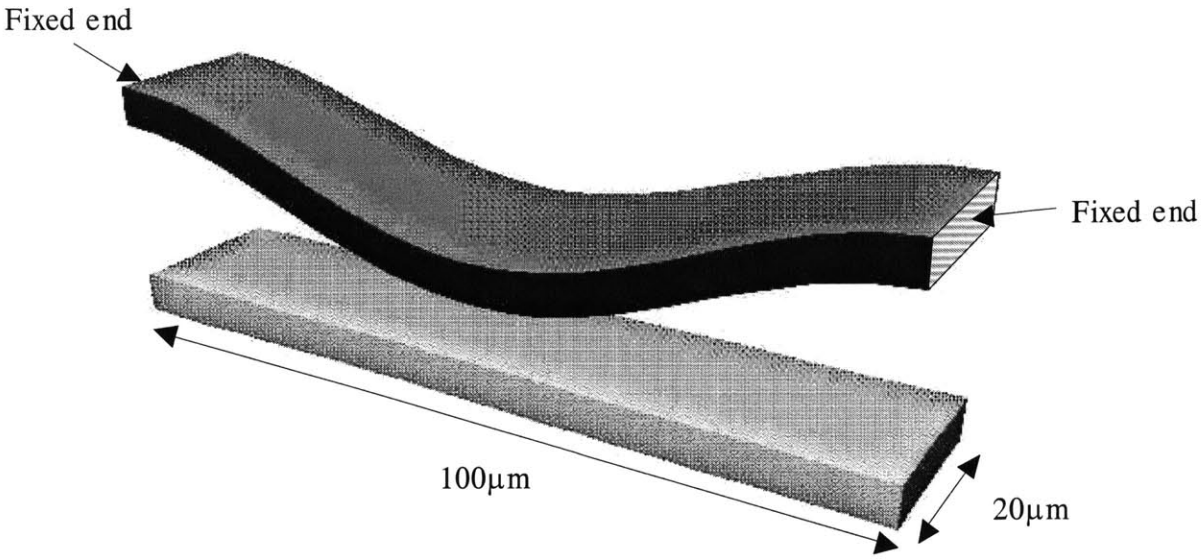

Figure 13 Polysilicon beam suspended 2μm above a ground electrode. The beam and electrode are identical in width, length and thickness (0.5μm). The polysilicon beam has a Young's modulus of 165Gpa, and a Poisson's ratio of 0.23.

4.1 Stress-stiffening

Stress stiffening occurs in a variety of MEMS devices when clamped structures bend to create displacements on the order of or greater than their cross-sectional thickness. This type of non-linearity is solely a function of the geometry of the device as it deforms and is not the result of any intrinsic non-linear material property such as Young's modulus. The clamped-clamped beam in Figure 13 exhibits stress stiffening. A beam of polysilicon, clamped on both its ends, is suspended above a ground electrode. When a voltage difference is applied between the beam and the ground electrode, the beam responds by bending [37] and also stretching along its axis (axial strain). For small amplitudes of motion, the axial strain component is negligible, and the mechanics of the beam can be described, in a discretized form, by a linear stiffness matrix as in Chapter 2:

$$\left[F_e\right]_N = \left[K\right]_{NxN}\left[y\right]_N \tag{45}$$

where Fe is a vector of the electrostatic forces, $[K]_{NxN}$ is an N by N stiffness matrix, and y is a vector of length N representing the positional state of the discretized beam with N degrees of freedom. Multiplying the above equation by $[P]^T_{NxN}$, where $[P]^T_{NxN}$ is the modal matrix (see Chapter 2), we can derive an equivalent representation in terms of linear mechanical mode amplitudes, q_i, the modal stiffness, k_i, and the electrostatic forces in modal co-ordinates f_{ei}:

$$\begin{bmatrix} f_{e1} \\ \vdots \\ f_{eN} \end{bmatrix}_N = \begin{bmatrix} k_1 & & \\ & \ddots & \\ & & k_N \end{bmatrix}_{NxN} \begin{bmatrix} q_1 \\ \vdots \\ q_N \end{bmatrix}_N \tag{46}$$

We note here that because the modal stiffness matrix is diagonal, there is no coupling between modes in the linear system. A mode, q_i, can only be excited by a corresponding electrostatic force f_{ei}.

When the amplitude of motion of the beam is on the order of its thickness or larger, the axial strain component is no longer negligible. The electrostatic forces must now not only bend the beam, but also stretch it, leading to a stiffer structure. The stiffness increases with the amplitude of motion, so the mechanical system is no longer linear, and equations (45) and (46) do not hold.

In addition to the increased stiffness, there are also two other important consequences to the axial strain, which leads to coupling between modes. The first is that the cross-section of the beam shrinks due to Poisson contraction [37], and the second is that the beam excites modes that reduce its curvature and hence minimize the axial strain [19]. We refer to these effects as "relaxation" because the corresponding motions allow the beam to "relax" to a lower energy state. These effects couple modes together mechanically which means that it is possible to excite a mode q_i without a corresponding electrostatic force f_{ei}.

Given that the CHURN process is well suited to deal with non-linear forces and coupling between modes, it would be appropriate to try the process on the mechanical energy domain. Gabbay [28] did just this, replacing capacitance calculations with strain-energy calculations as shown in Figure 14, then finding mechanical forces from a strain energy function:

$$f_i^{mech} = \frac{\partial U_{mech}}{\partial q_i} \tag{47}$$

Unfortunately, the process failed to capture the non-linearity accurately. In Figure 15 we plot the mode 1 displacement for the beam as a function of applied voltage and compare it to the linear mechanics macro-model and the CHURN based nonlinear mechanics macro-model. The linear mechanics macro-model does not capture the additional stiffness of the stress stiffening in the real device, whereas the CHURN macro-model produces a model that is much stiffer than the real device.

Gabbay attributed the inaccuracy of the CHURN macro-model to its inability to capture the relaxation of the device as it stretches. This is because the CHURN process constrains the beam to motions only in the chosen modes, which are not the modes in which relaxation occurs. In Appendix C we demonstrate, in much greater detail, how modal coupling leads to the failure of the CHURN process [30].

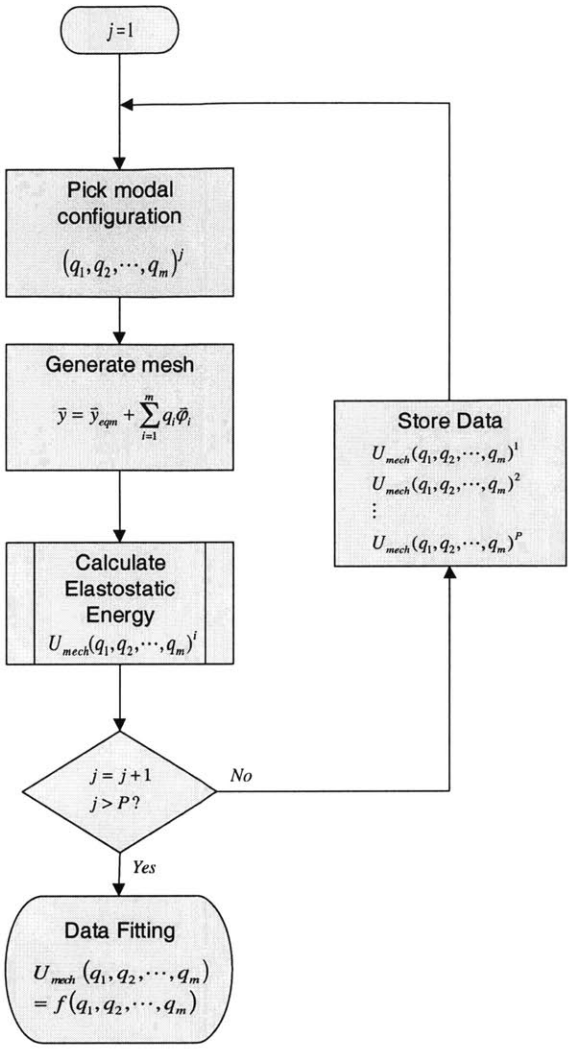

Figure 14 CHURN process adapted for elastostatic energy domain. U_{mech} is the elastostatic energy calculated using a mechanical FEM solver, such as MemMech [29].

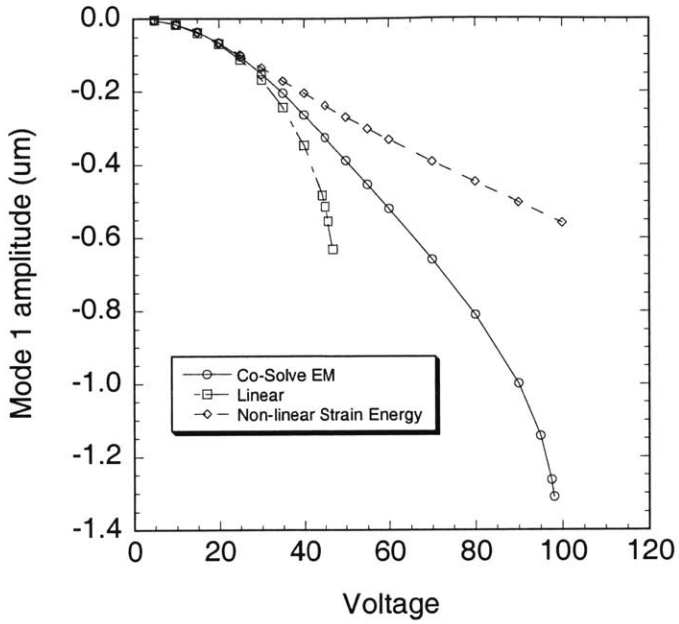

Figure 15 Plot comparing results of fully meshed Co-Solve EM simulations to linear and non-linear CHURN based macro-models. The linear macro-model has larger deflection at the same voltage than the full FEM simulation, while the non-linear macro-model has smaller deflections. The stiffness of the mechanical structure is not captured accurately in both reduced-order models.

4.2 Poisson contraction

Poisson contraction is one of the mechanisms of relaxation that is not captured by the CHURN process due to constraints. To understand the effects of constraining Poisson contraction, it is convenient to separate the axial stretching component from the bending component of the beam deflection. Consider the beam shown in Figure 16 with an applied axial stress, σ_x, and unconstrained in the y and z directions (stresses σ_y and σ_z are both zero). The beam responds with a strain in the x direction, ε_x, but also strains in the y and z directions, ε_y and ε_z due to Poisson contraction. The general response of the beam to stresses σ_x, σ_y and σ_z is given by:

$$\begin{bmatrix} \varepsilon_x \\ \varepsilon_y \\ \varepsilon_z \end{bmatrix} = \frac{1}{E} \begin{bmatrix} 1 & -\nu & -\nu \\ -\nu & 1 & -\nu \\ -\nu & -\nu & 1 \end{bmatrix} \begin{bmatrix} \sigma_x \\ \sigma_y \\ \sigma_z \end{bmatrix} \tag{48}$$

For a given change in length δL in the x direction, the strain is $\frac{\delta L}{L}$. The corresponding applied stress is $E\frac{\delta L}{L}$, and strains in the y and z directions are both $-\nu\frac{\delta L}{L}$. Now, consider the same change in length δL in the x direction, but constraining Poisson contraction by preventing relaxation in the y and z directions (constraining ε_x and ε_y to zero). Solving equation (48), the required x directed stress is $E\frac{\delta L}{L}\frac{(1-\nu)}{(1-2\nu^2-\nu)}$. This is greater than the unconstrained stress by $\frac{(1-\nu)}{(1-2\nu^2-\nu)}$. For Polysilicon, which has a Poisson ratio of 0.23, the constrained beam requires a 16% greater stress than the unconstrained beam for the same strain. Hence, the constrained beam is stiffer than the unconstrained beam.

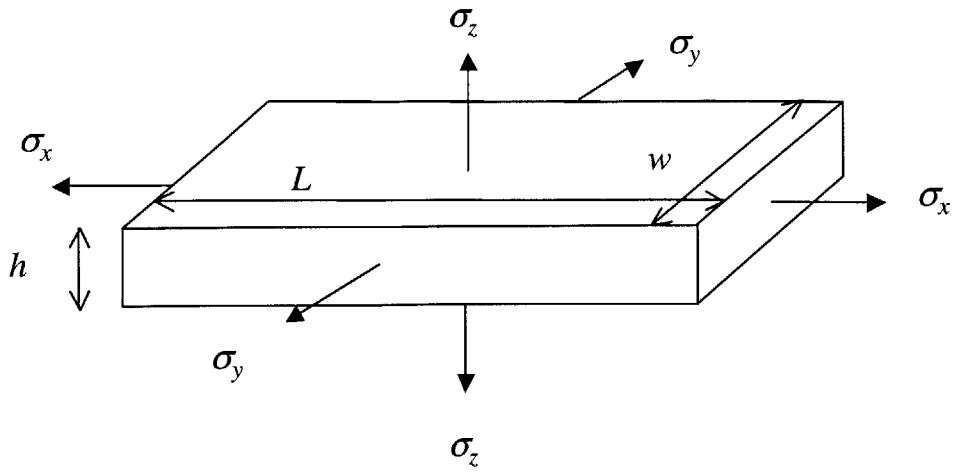

Figure 16 Block of material with isotropic Young's modulus, E, and a Poisson ratio of v. The block has dimensions of length, L, width, w, and thickness, h. Stress in the x, y, and z directions are σ_x, σ_y, and σ_z respectively. Strains in the x, y, and z direction are ε_x, ε_y, and ε_z respectively.

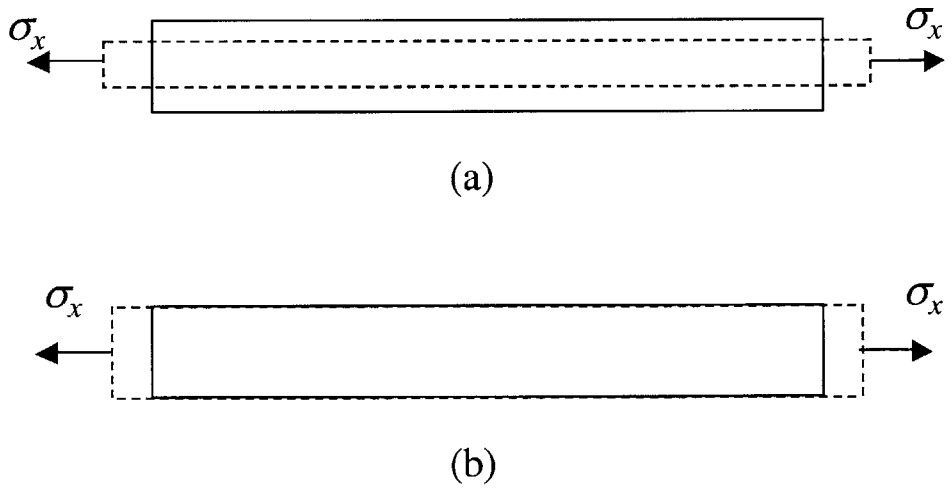

Figure 17 Side view of block, with x directed stress. (a) No imposed constraints on the motion. Poisson contraction takes place. (b) Zero strain constraint imposed in the y and z directions.

4.3 Relaxation strategies

Gabbay [28] proposed that allowing some degree of relaxation at the nodes in the finite element mesh, while still retaining a good approximation of the modal superposition, would reduce the error in stiffness. For the clamped beam example in the previous sections he explored two constraint strategies. First, he constrained only the surface nodes (all surfaces) according to modal superposition, allowing the remaining internal nodes free to relax. Second, he constrained only the nodes on the bottom surface of the beam (facing the ground electrode) according to modal superposition, allowing the remaining nodes free to relax. The results are shown in Figure 18 It is clear that both strategies reduced the error in the stiffness. The second strategy, with the least constrained nodes, did better than the first but still failed to capture the stiffness of the beam accurately.

Mehner [19] took the relaxation strategy further and implemented a successful solution for a restricted, but useful, class of MEMS devices. He looked at devices that had a dominant direction of motion (in the case of the beam, the z direction), and in addition had a clearly defined neutral surface. He constrained only the nodes on the neutral surface, according to modal superposition, but only in the dominant direction. That is, the nodes along the neutral surface had their z position constrained, but were free to relax in the x and y directions.

Both the strategies above deviate from strict adherence to modal superposition. The position of a device is no longer strictly constrained to the original set of m modes. The degree of constraint controls the success of these strategies, and is dependent on the specific geometry of a device. This motivates us to find a more general approach for finding an accurate strain energy function.

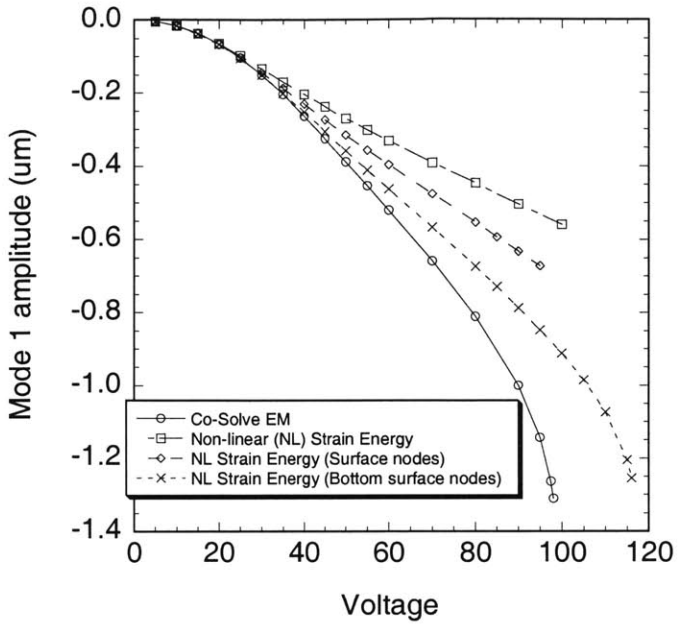

Figure 18 Plot comparing results of fully meshed Co-Solve EM simulations to macro-models utilizing different relaxation strategies. The CHURN based NL strain energy macro-model has the largest deviation from the Co-Solve results. The model with only surface nodes constrained according to modal superposition shows improvement, and further improvement is seen by the model with only its bottom surface constrained.

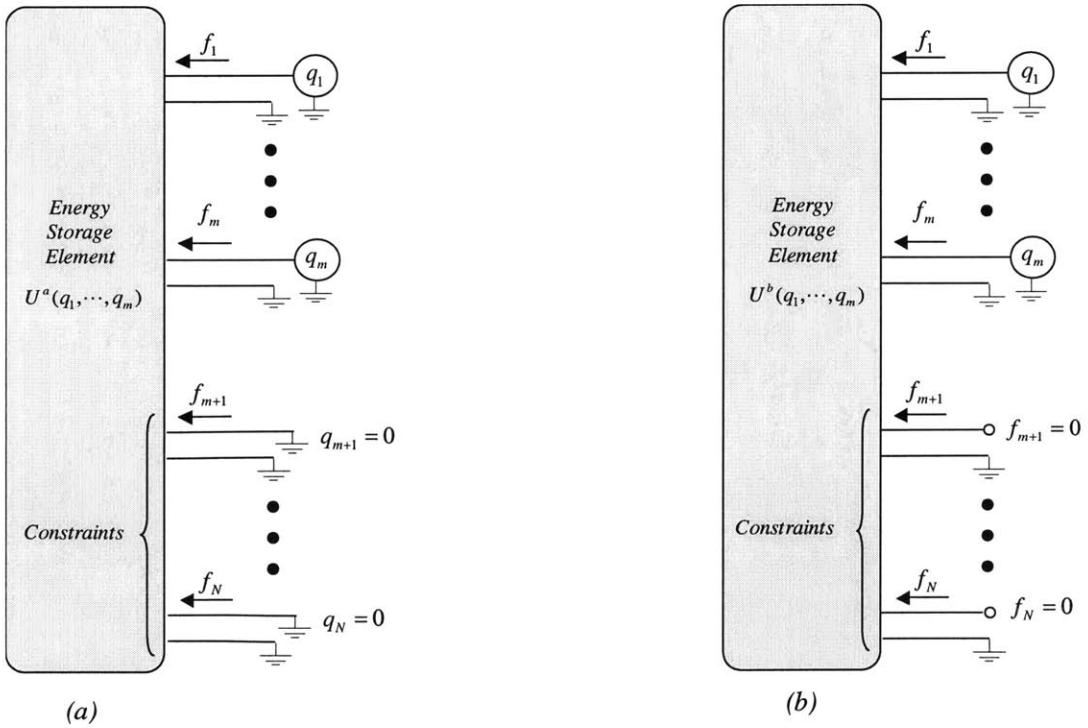

Figure 19 N mechanical port energy storage elements. (a) N-m modes are constrained to zero amplitude. (b) N-m modal forces are constrained to zero amplitude.

4.4 Strain energy functions

Consider the two N port strain energy storage elements in Figure 19. The modal force, f_i, flowing into the port and the modal amplitude, q_i, across the port, defines each port. Without any constraints, these elements represent the stored energy in a finite element mesh with N degrees of freedom. Each element, though, has N-m imposed constraints. Element (a) has N-m modes constrained to zero modal amplitude, and element (b) has N-m modes constrained to zero modal force, f_i. Given the constraints, the stored energy in each of the elements, $U_a(q_1,\cdots,q_m)$ and $U_b(q_1,\cdots,q_m)$, can be uniquely identified by only m modal amplitudes, $\{q_1,\cdots,q_m\}$. These are two examples that illustrate how constraints are used to reduce the order of a system (assuming, of course, that the constraints are appropriate to the real system).

The constraints on element (a) are exactly those that are applied when modal superposition is used to reduce the order of a system. Motion is restricted to m selected modes, with the remaining modes constrained to zero amplitude. This is an approximation for a device that displays significant excitation in only m modes. The CHURN process allows us to find the stored energy of the system, $U_a(q_1,\cdots,q_m)$, given these constraints

The accuracy of the macro-model in Figure 19 (a), however, is dependent on the validity of the constraints, and it was shown in the previous section how they did not reflect those of the real system well.

If the real device was linear, and displayed significant excitation in m modes, it implies that only the corresponding m modal forces were significant. Thus, another approximation to this device is to explicitly set the remaining modal forces to zero. That is, constrain modal forces instead of modal amplitude. Only forces $\{f_1,\cdots,f_m\}$ now act on this constrained system as in Figure 19 (b). For the linear device, the modal force constraints produce the same results as modal amplitude constraints. However, when modes are coupled together, there is a significant difference.

Consider the equilibrium state for the two elements in Figure 19 when external forces $\{f_1,\cdots,f_m\}$ are applied, and the element is non-linear with modal coupling. Element (a) has constrained modes, so the modal forces adjust themselves to maintain this constraint.

$$\{f_1,\cdots,f_m\}\rightarrow\{f_1,\cdots,f_m,f_{m+1},\cdots,f_N\},\{q_1,\cdots,q_m,q_{m+1}=0,\cdots,q_N=0\}$$

In the final state, a small virtual displacement δq_i, in one of the higher order modes (i>m), means that the constraint force f_i does work $f_i\delta q_i$. Thus, this element is not at an energy minimum with respect to the higher order modes and is not fully relaxed.

Element (b) has constrained modal forces, so the modal amplitudes adjust themselves to maintain this constraint.

$$\{f_1,\cdots,f_m\}\rightarrow\{f_1,\cdots,f_m,f_{m+1}=0,\cdots,f_N=0\},\{q_1,\cdots,q_m,q_{m+1},\cdots,q_N\}$$

The same virtual displacement, $\delta q_i(i>m)$, in this case does no work as the modal force f_i is zero. All other modal forces, $\{f_1,\cdots,f_m\}$, also do no work over this displacement (see Appendix B). Thus, this element is at an energy minimum with respect to the higher order modes and allowed relaxation to take place.

The above result suggests that the strain energy for element (b) is a better approximation to that in the real device because Poisson contraction and other forms of modal coupling are allowed to occur through relaxation.

Finding the strain energy for element (a) is relatively simple using the CHURN process. Recall that the CHURN process had four main tasks

1) Pick configuration $\{q_1,...,q_m\}$
2) Generate the mesh shape with this configuration and associated constraints.
3) Caluclate strain energy
4) Fit strain energy data with an analytical function.

The shape of a device, for a given configuration $\{q_1,\cdots,q_m\}$ is trivial to calculate using modal superposition. However, for element (b), the shape for the same configuration $\{q_1,\cdots,q_m\}$ is not as simple because the higher order modes have a contribution. Ideally, we should have a technique of specifying a configuration and calculating the associated shape directly with the zero force constraints. From this point of view, it appears that the relaxation strategies of Gabbay and Mehner were attempts at such a technique. However, their use of a modified modal superposition, combined with nodal relaxation, neither guaranteed a particular configuration, $\{q_1,\cdots,q_m\}$, nor zero force constraints. They were only approximations that worked for a restricted class of problems.

We adopt a different strategy that does not utilize modal superposition. We can specify the configuration of element (b) by either specifying mode amplitudes $\{q_1,\cdots,q_m\}$, or equivalently modal forces $\{f_1,\cdots,f_m\}$. There is a one to one correspondence between these amplitudes and forces, albeit non-linear. Figure 20 shows how we use modal forces to generate a strain energy function. We calculate the linear reaction forces at each mesh node, F_i, associated with displacing the structure into mode shape φ_i. We then apply a superposition of these modal forces as a load on the device and calculate the resulting displacement and strain energy. Note that this guarantees the zero modal force constraint on the higher order modes. To determine the mode amplitudes $\{q_1,\cdots,q_m\}$ that correspond to the modal forces $\{f_1,\cdots,f_m\}$ we project the resulting shape back onto the modes:

$$q_i = \frac{\left(\vec{y} - \vec{y}_{eqm}\right)^T [M]_{NxN} \vec{\varphi}_i}{\varphi_i^T [M]_{NxN} \vec{\varphi}_i} \tag{49}$$

$$\vec{y} = \vec{y}_{eqm} + \sum_{i=1}^{m} q_i \vec{\varphi}_i + \varepsilon \tag{50}$$

where we make use of the fact that modes are orthogonal over the mass matrix.

Here, ε is the contribution of the higher order modes associated with relaxation. We repeat the above procedure to build up a data set of strain energy for various modal force, or equivalently modal amplitude configurations, finally fitting the results to a polynomial in mode amplitudes.

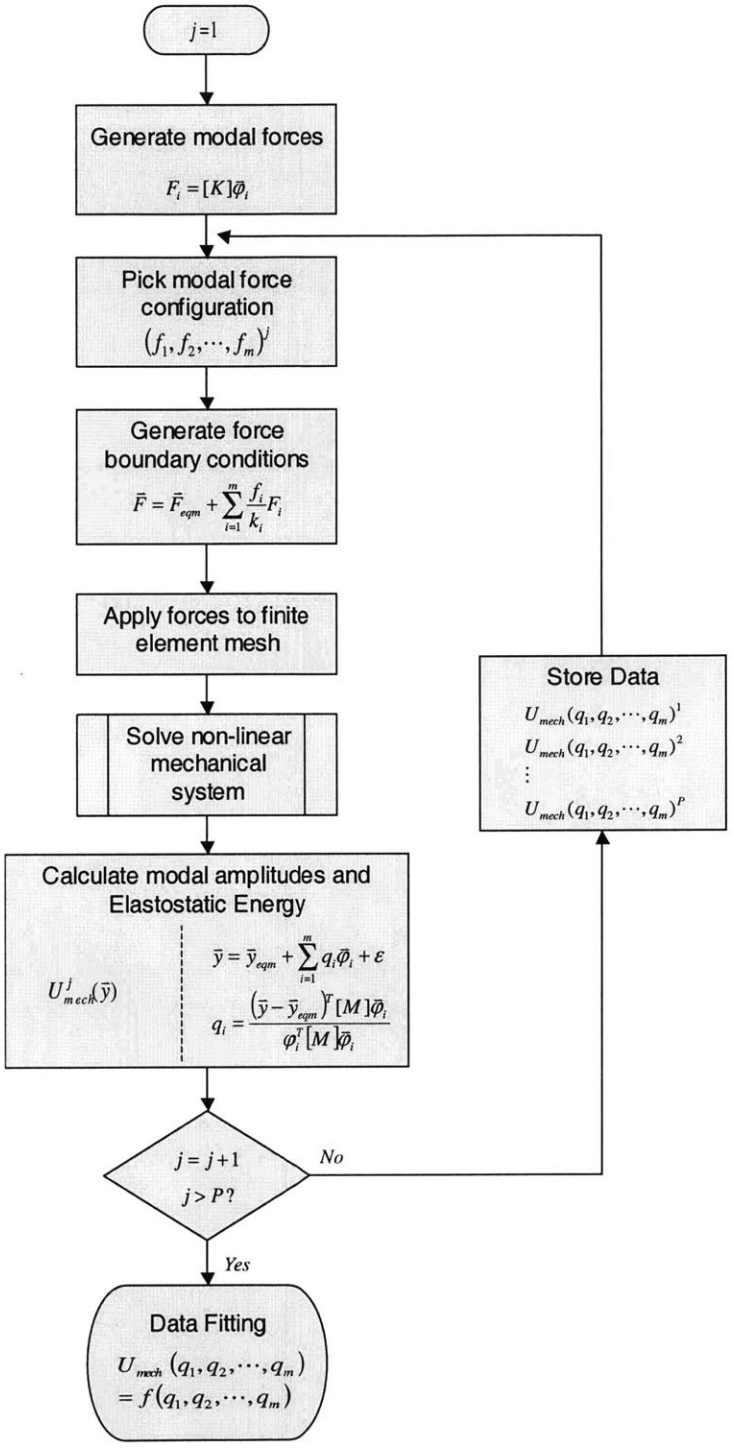

Figure 20 Methodology for creating strain energy function, U_{mech}, with zero modal force constraints on higher order modes.

4.5 Energy domain coupling

Recall that our reduced-order modeling methodology coupled multiple energy domains together and derived its equations of motion using the Lagrangian:

$$L(q,\dot{q},t) = T(q,\dot{q},t) - U(q,\dot{q},t) \tag{51}$$

where $T(q,\dot{q},t)$ is the kinetic energy of the system, and $U(q,\dot{q},t)$ is the sum of the potential energies of all the energy domains in the system. The CHURN process generated energy (or co-energy) functions that were inserted into the Lagrangian. The modal co-ordinates were consistent between energy domains, so the state $\{q_1,\ldots,q_m\}$ referred to the same shape in each energy domain, as it was always generated by strict modal superposition. However, as we saw in the previous section, the shape for the modal-force based model associated with state $\{q_1,\ldots,q_m\}$ is different by an error, ε. Ideally, all the energy domains should use the same state variables, associated constraints, and shapes.

There are, however, benefits to continuing use of strict modal superposition on non-mechanical energy domains. The kinetic energy of the system is easy to calculate when the motion in the higher order modes is constrained.

$$T = \sum_{i=1}^{m} m_i \dot{q}_i^2 \tag{52}$$

In addition, computing the position of the mesh, given a set of modal amplitudes is trivial.

$$\vec{y} = y_{eqm} + \sum_{i=1}^{m} q_i \vec{\varphi}_i \tag{53}$$

Mehner's work [19] demonstrates that for small positional deviations, ε, in the higher order modes the electrostatic potential energy will change negligibly. His successful results also demonstrate that the kinetic energy obtained by equation (52) does not contribute a significant error to the equations of motion. Hence, for ease of implementation, we continue to employ the CHURN process to generate the electrostatic co-energy function, use the modal-force methodology to generate the strain energy function, and use equation (24) to compute the kinetic energy.

4.6 Implementation

The CHURN algorithm presented in Chapter 2, for creating macro-models was adapted to include the modal-force based strain energy function. An overview of the modified algorithm is shown in Figure 21. The data generation for both the electrostatic and elastostatic energy domains was implemented in MEMCAD [29] using MemCap and MemMech respectively. Polynomials for the strain energy function and rational polynomials for the electrostatic co-energy were fitted using the Levenberg-Marquardt [38] algorithm in MATLAB [32]. Finally, the equations of motion were implemented in the system level simulator, SABER [7].

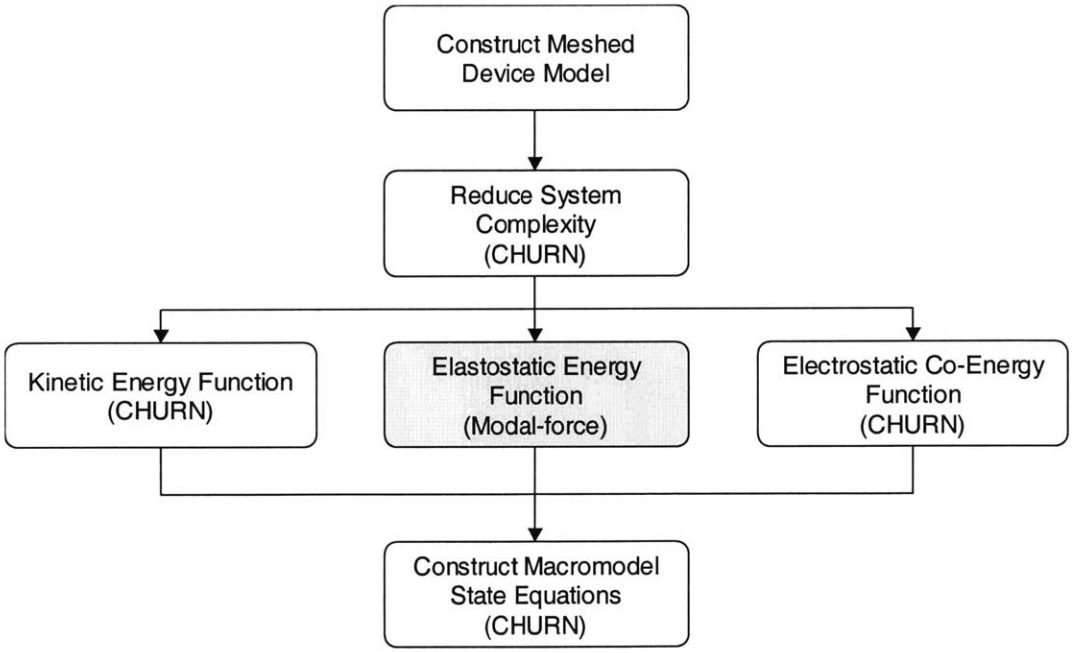

Figure 21 Modified CHURN macro-model generation algorithm. The shaded box represents the modification for creating an accurate strain energy function using modal forces.

4.7 Clamped-clamped beam

Our first example is the clamped-clamped beam described previously in this chapter. We compare three reduced-order model solutions with 3D meshed, simulations performed in MEMCAD (Figure 22). The CHURN process produces a macro-model that is stiffer than the real structure. The linear mechanics macro-model, in contrast, is less stiff than the real structure. Our macro-model follows the MEMCAD simulations well, and is within 5% of the MEMCAD solution at 90% of the "pull-in" [33] voltage when the beam is well into the stress-stiffening regime.

The generation of the data set for this example, and other devices, involved selecting a representative set of sample points in the mode space. The CHURN process has an algorithm for selecting such a set of points. Unfortunately, this algorithm must be used with caution in the modal-force formulation. We cannot sample a given point in mode space directly; we can only specify forces necessary to displace a structure to the required shape. Since the relationship between forces and displacement is unknown to begin with, the algorithm breaks down. Our solution is to approximate the given forces by assuming a linear system, and then adaptively improving the approximation as the data set increases in size. Currently this is done manually, but the task could be automated in the future.

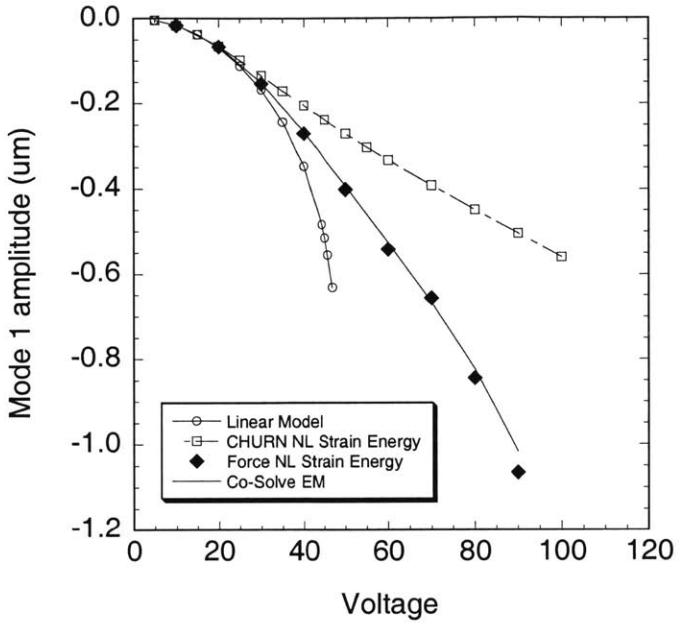

Figure 22 Plot of mode 1 amplitude vs. applied voltage. Results from 3D FEM coupled simulation performed using MEMCAD's Co-Solve EM simulation tool are compared to three Macromodels.

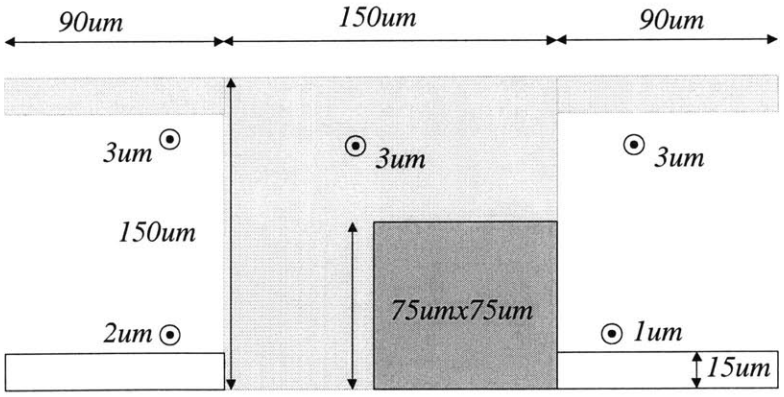

Figure 23 Asymmetrically supported plate. The actuation electrode is located 6um below the bottom of the plate. The plate and its supports have a Young's modulus of 165Gpa, and a Poisson's ration of 0.23.

4.8 Asymmetrically supported plate

In this section we demonstrate the modal force methodology on an asymmetrically supported and actuated plate (Figure 23). The plate has supports of different lengths and thickness, and an off-center actuation. The example shows that the methodology is applicable to a more general structure, one without significant symmetry, and in particular, without a clearly defined neutral plane.

The first six elastic modes were used to model this device. 200 mechanical simulations, and 200 electrostatic simulations were performed to generate data sets for the elastostatic energy and the electrostatic co-energy functions. However, both functions used polynomials with approximately 90 fitting coefficients. This indicates that the number of simulations required in the data sets could significantly be reduced. The minimum number of data points that are required to accurately construct the energy functions is a topic for further investigation.

The time taken for the construction of the macromodel was approximately 10 hours on a SUN Ultra 30 workstation running at 200Mhz. Simulations performed using the macromodels in the system level simulator, SABER, took less than 10 seconds to complete.

Figure 24 is a plot of the first mode amplitude against the applied voltage. Stress-stiffening is significant at 200V and we observe the divergence of the linear model from the MEMCAD solution. The force model, however, is accurate to within 1% at 200V. Figure 25 shows the response of modes 2,3 and 4 to the applied voltage. The force model is within 5% of the MEMCAD solution at 200V when the deflection is on the order of 1μm, the thickness of the thinnest supporting beam.

We make a note here that the macromodel was significantly inaccurate at very small amplitudes (<10nm). We believe this is a result of errors in the method of projecting shapes back onto the modes during the data set construction. The current projection method cannot resolve small amplitudes in modes if one of the modes has large amplitude.

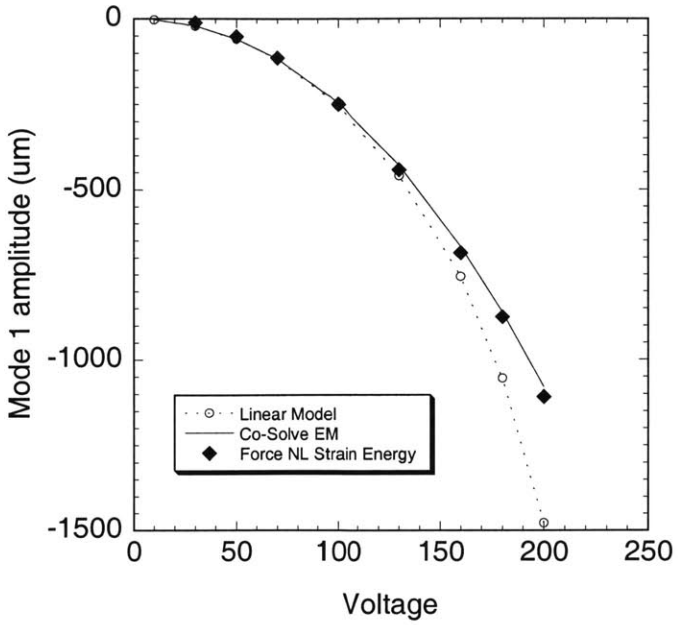

Figure 24 Mode 1 amplitude vs. applied voltage for the asymmetric plate.

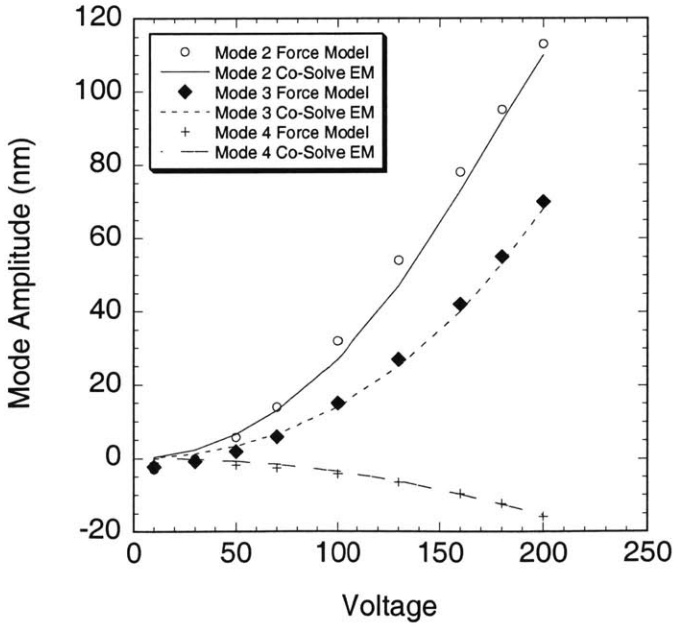

Figure 25 Mode 2,3, and 4 amplitudes vs. applied voltage for the asymmetric plate.

4.9 Summary

In this chapter we explored the issue of stress stiffening in MEMS devices. Stress stiffening occurred when clamped structures exhibited displacements on the order of or greater than their cross-sectional thickness. The original CHURN process was unable to capture this non-linearity accurately, creating models that were significantly stiffer than real devices. A mathematical explanation of this failure was presented in Appendix C.

We showed how constraints imposed during the modeling process led to the additional model stiffness. These constraints, the result of the truncated modal superposition approximation, did not accurately reflect the real constraints on the system. The real system was not constrained to zero amplitude in the higher order modes.

We suggested that zero force constraints on the higher order modes were a better approximation. These force constraints still enabled model order reduction through the use of a truncated set of modes, but allowed the necessary relaxation in the higher order modes. We implemented this approach in the MEMCAD framework and presented successful results for a clamped-clamped beam, and an asymmetrically supported plate.

We also showed that the modal force methodology was compatible with the CHURN process for other energy domains. Thus, models could be created using the CHURN methodology for magnetic and electrostatic forces, and using the modal force methodology for the non-linear mechanical forces.

5 Automation

This chapter explores the issues relating to applying modal reduced-order models to practical problems of interest in MEMS. The focus is placed on electromechanical systems, but the techniques developed here could be applied to magentomechanical, or other types coupled systems.

A MEMS designer is typically interested in obtaining a dynamic reduced-order model with the least degree of manual interaction in the model generation process. It is the final model, and not the mechanism of model generation that is useful to a designer. In Gabbay's CHURN process, the designer is involved in selecting the relevant modes, defining maximum and minimum mode amplitudes for each mode, selecting polynomial order for energy functions, and specifying typical actuation voltages for an initial coupled simulation. One objective in this chapter is to present heuristic techniques that eliminate or minimize the degree of designer intervention in the model generation process.

We begin this chapter by extending the CHURN process to model multi-electrode devices. We then present our approach to automatically selecting relevant modes, and finding modal amplitude bounds for these devices. An approach to eliminating full 3D Co-Solve EM coupled simulations is described, followed by an explanation of our implementation of the generation of a capacitance function. Finally, we apply our model generation algorithm is applied to model a real, microfabricated high frequency filter, and compared the results to measured data. The aim of this exercise is to demonstrate the validity of our macromodeling methodology and also provide a practical example of constructing a macromodel. An example of its ability to model more complex filters is also presented.

5.1 Multi-electrode systems

Realistic MEMS devices have several electrodes for the actuation and sensing of motion in its mechanical components. The original CHURN process, however, is limited to two

electrode systems because the electrostatic co-energy and forces in that formulation are a function of a single capacitance.

$$U_e^* = \frac{1}{2} C V^2 \tag{54}$$

$$f_i = \frac{1}{2} \frac{\partial C}{\partial q_i} V^2 \tag{55}$$

It is relatively straightforward to extend the co-energy formulation to handle the multiple self- and mutual- capacitances of a multi-electrode electrostatic device. These capacitances describe the relationship between the charge and potentials on the device electrodes. Consider the four electode electrostatic system in Figure 26

$$\begin{bmatrix} Q_1 \\ Q_2 \\ Q_3 \end{bmatrix} = \begin{bmatrix} C_{11} & C_{12} & C_{13} \\ C_{21} & C_{22} & C_{23} \\ C_{31} & C_{32} & C_{33} \end{bmatrix} \begin{bmatrix} V_1 \\ V_2 \\ V_3 \end{bmatrix} \tag{56}$$

Q_i is the charge on the i^{th} conductor, C_{ij} is the capacitance between i^{th} and j^{th} conductors, and V_i is the potential of the i^{th} conductor. The co-energy for this system is:

$$U_e^* = \sum_{j=1}^{3} \sum_{k=1}^{3} \frac{1}{2} C_{jk} V_j V_k \tag{57}$$

The electrostatic forces for modal co-ordinates q_i follows from the co-energy and is:

$$f_i = \sum_{j=1}^{3} \sum_{k=1}^{3} \frac{1}{2} \frac{\partial C_{jk}}{\partial q_i} V_j V_k \tag{58}$$

To obtain analytical representations for the above forces, the CHURN process is modified to generate analytical representations for each entry in the capacitance matrix. As the process iterates through the data generation, a capacitance matrix is calculated and stored, instead of a single capacitance. Polynomials for each entry in the matrix are then fit to this data. Since the capacitance matrix is symmetric, only the entries in the top half require fitting in practice.

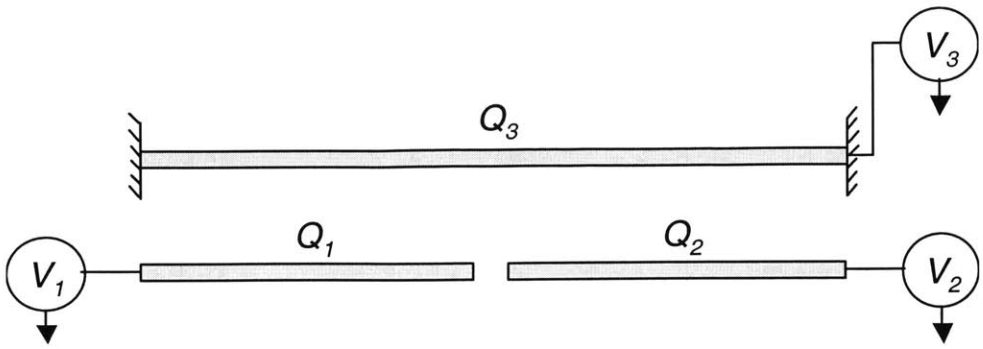

Figure 26 Four-electrode system containing a fixed-fixed beam mechanical element. Three electrodes are shown, with the fourth electrode taken to be an infinite distance away.

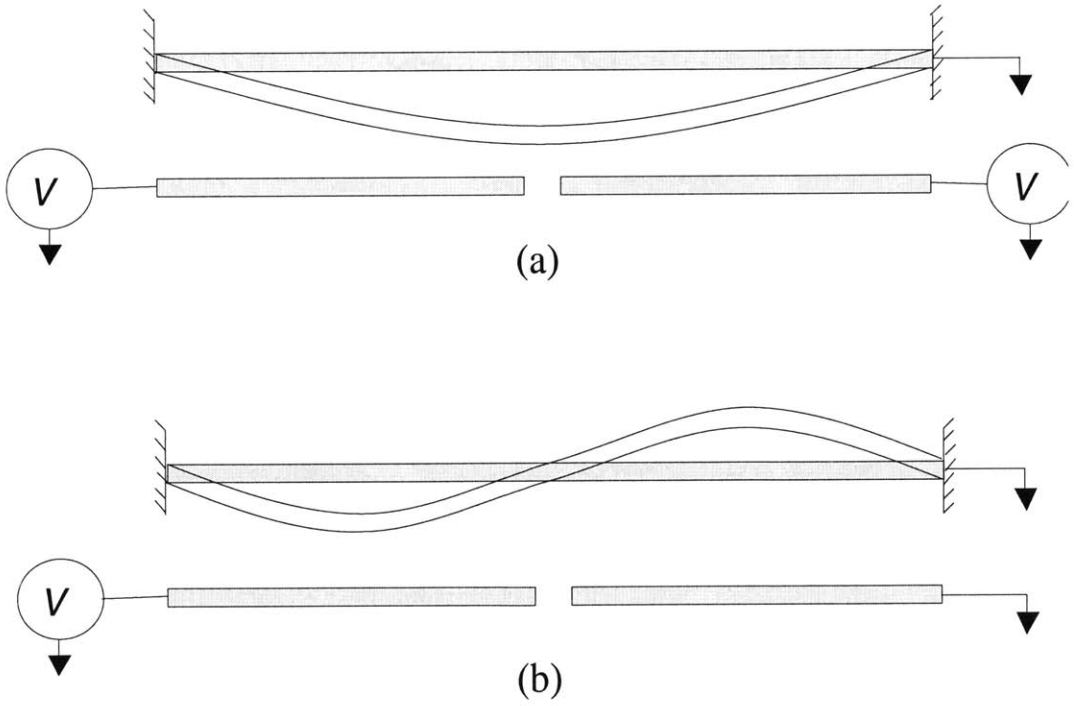

Figure 27 Actuation of fixed-fixed beam with different voltage excitation patterns. (a) V_1 and V_2 have equal voltage V. (b) V_1 has voltage V, and V_2 is grounded.

5.2 Mode selection

The task of selecting the relevant modes for model order reduction increases in complexity for multi-electrode systems. In the CHURN process, a designer is required to determine which modes are relevant, guided by the results of a single Co-Solve EM coupled simulation. This simulation is intended to be a representative example of device operation and the results are presented as an ordered list of mode amplitudes:

Voltage = 30V	
Mode	Amplitude
3	-1.6334500
1	0.0026733
⋮	⋮
20	0.0000033

Table 1 Example modal excitations for a Co-Solve EM coupled simulation. Only the mode amplitudes for the top 20 modes are computed for this list. Experience shows that only the low order modes (under mode number 10) are required to accurately model typical MEMS devices.

The designer now decides how many modes, going down from the top of this list, to use in the macromodel. For an m^{th} order model, the top m modes are selected.

We first extend this mode selection procedure to the more complex multi-electrode case. Unlike systems with two independent electrodes, it is not only the spatial location and geometry of the electrodes that primarily determine mode selection, but also the pattern of voltages applied to these electrodes. To illustrate this point, consider the example in Figure 27. When V_1 and V_2 are equal, only the symmetric modes of the beam are excited, but if V_2 is zero, additional anti-symmetric modes are also excited. This indicates that multiple Co-Solve EM simulations are now required to guide a designer in selecting modes, and in addition, the simulations should be chosen to be representative of the typical voltage excitation patterns of the device when it is in use.

We perform separate Co-Solve EM simulations for each voltage excitation pattern specified by a device designer, and the resulting modal amplitudes are tabulated (Table 2). We select the m modes with the highest absolute modal amplitudes across all the simulations for use in the macromodel. Another possible selection criterion is to take the root mean square of mode amplitude across the simulations and pick the m highest values.

Mode	Excitation pattern 1	Excitation Pattern 2	Excitation Pattern 3	Maximum Amplitude
1	0.0026733	0.2026733	-1.0023723	1.0023723
2	1.4334500	0.6334500	-0.3456823	1.4334500
⋮	⋮	⋮	⋮	⋮
20	0.0000033	0.0004533	0.0000413	0.0004533

Table 2 Example modal excitations of Co-Solve EM simulations for designer specified excitation voltage excitation patterns.

It is desirable to automate the mode selection procedure and completely eliminate the role of the device designer in selecting typical excitation patterns. We have implemented such an approach. We treat the system as if it were linear and find an effective "impulse response" by applying a small voltage to each electrode in turn, keeping the remaining electrodes grounded. One Co-Solve EM simulation is performed for each of these excitation patterns, and the modes are then selected from this group. The designer is now only responsible for selecting the model order, m.

The main issue with this technique is that it is not guaranteed to pick out the set of m modes that most accurately model the device under typical operating conditions. When a device is operated only in a particular excitation pattern that isolates certain modes, the modes excited by other excitation patterns are not as relevant to the macromodel. In the example in Figure 27 (a), only the symmetric modes are required to model the device, but our "impulse response" methodology is likely to select both symmetric and anti-symmetric modes. However, such modal isolation is not typical in MEMS, and in the event that a device is expected to operate under such conditions, there is always the option of returning to the manual selection of voltage excitation patterns.

5.3 Mode amplitude bounds

In CHURN, once the relevant modes are selected, a designer is required to specify a set of mode amplitude bounds. For example, for a device modeled with two modes, q_1 and q_2, a designer specifies the maximum absolute amplitude of each mode, $|q_1|_{\max}$ and $|q_2|_{\max}$. These bounds define a box in mode space (see Figure 28) within which the device is expected to operate. CHURN generates an accurate electrostatic co-energy function by taking representative samples of the capacitance within these bounds. In selecting the modal bounds, a designer is guided in part by the amplitudes of the modes in the Co-Solve EM simulation that was performed to select the relevant modes.

A designer, although unlikely to intuitively know specific modal bounds within which a device is expected to operate, is likely to know a maximum expected amplitude of deflection of the device (a gap height, for example). We use a heuristic algorithm to automatically define bounds for the mode amplitudes based on a maximum expected deflection, $d_{\max}$.

An ordered list of the m selected maximum mode amplitudes is first generated from Table 2. These amplitudes, after they are scaled such that the first amplitude in the list is $d_{\max}$, form our modal bounds. The amplitudes from Table 2 in essence act as a guide to the relative excitation of the various modes to each other. An additional criterion that $\left|\sum_{i=1}^{m} q_i\right| < d_{\max}$ is also added to bound the region. Table 3 shows the bounds that result from this algorithm when applied to the example data in Table 2 (two modes are selected). The region in which the device is expected to operate is shaded in Figure 29.

Mode	Maximum Amplitude	Scale to unity	Scale to dmax (modal bounds)
2	1.4334500	1.0000000	$d_{\max}$
1	1.0023723	0.6992726	$\sim 0.7 d_{\max}$

Table 3 Calculation of modal bounds based on a maximum displacement, $d_{\max}$.

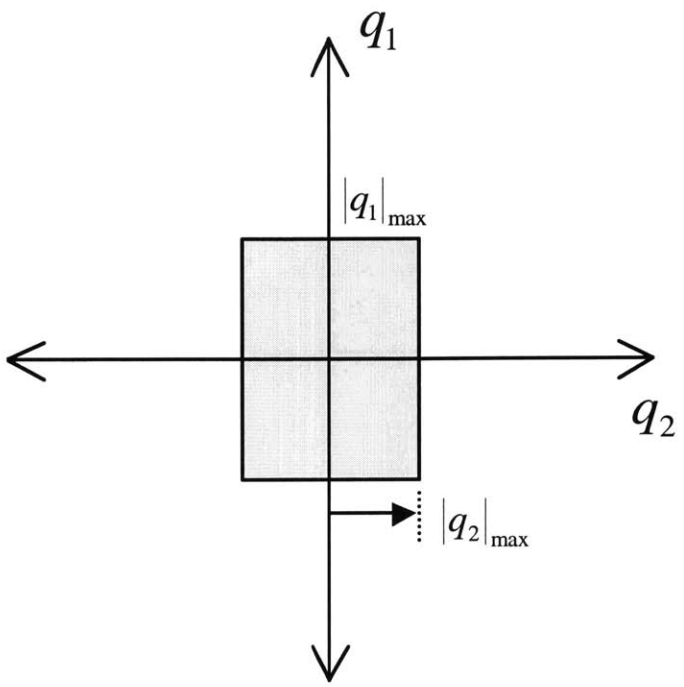

Figure 28 Operating range as it is defined in CHURN.

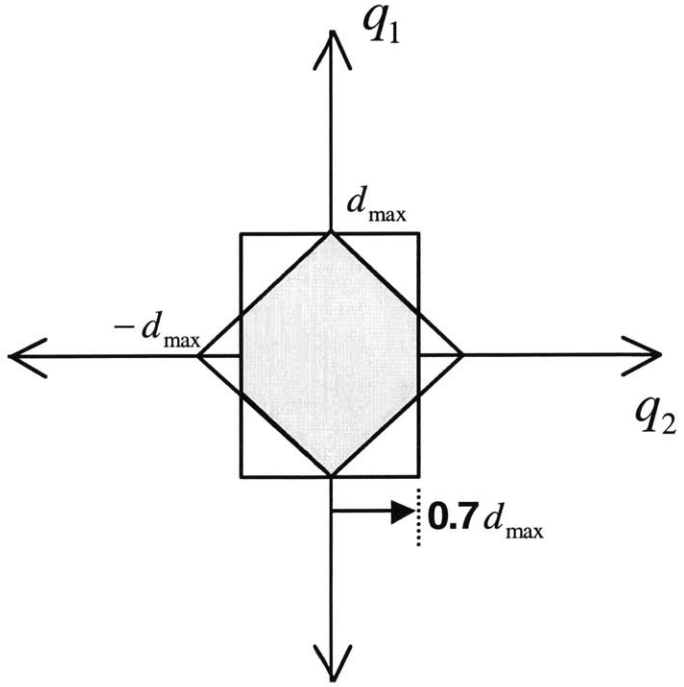

Figure 29 Operating range for the modified CHURN process. Bounds are a function of the maximum expected deflection, d_{max}, specified by a designer.

5.4 Polynomial fitting

One of the least explored issues in this thesis concerns the task of creating energy functions by fitting polynomials or rational polynomials to sampled data. Although we have found success in using these functions, several questions remain to be answered in future work. What is the minimum number of samples necessary to create an accurate energy function? Is there a robust error estimate that may be used to qualify the fit, and more importantly, qualify the accuracy of the calculated forces? Are there better and more robust analytical representations than standard polynomials, or rational-polynomials?

Gabbay used rational polynomials to represent the capacitance function in his models. This was based in part on the notion that the function should have a form that captures the non-linearity expected from the capacitance. This expected non-linearity is exemplified by a set of parallel plate capacitors where the capacitance takes the form (neglecting the contribution of fringing fields):

$$C = \frac{\varepsilon_0 A}{d_0 - x} \tag{59}$$

where A is the area of the plates, and d_0 is the nominal distance between the plates, and x is the displacement of a capacitor plates away from d_0. Gabbay noted that x corresponds most with the mode amplitudes, and thus, justifies having a polynomial in the denominator of the fitting function. In our work, however, we have successfully used standard multivariate polynomials to model the capacitance. Standard polynomials are particularly effective for modeling the capacitance when devices operate below the "pull-in" threshold. For the parallel plate capacitor, this threshold is not exceeded when the device amplitude is below a third of the gap. Figure 30 illustrates a third and fourth order polynomial approximation to the capacitance in equation (59). In Figure 31 we plot the error in the electrostatic force computed from the two polynomial approximations.

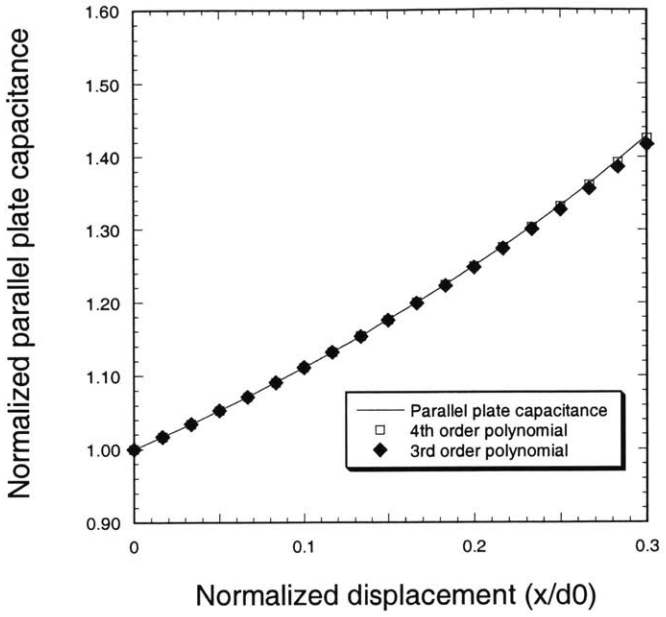

Figure 30 Polynomial approximations to the capacitance of a parallel plate capacitor. The capacitance and displacement are normalized to the nominal capacitance and gap respectively.

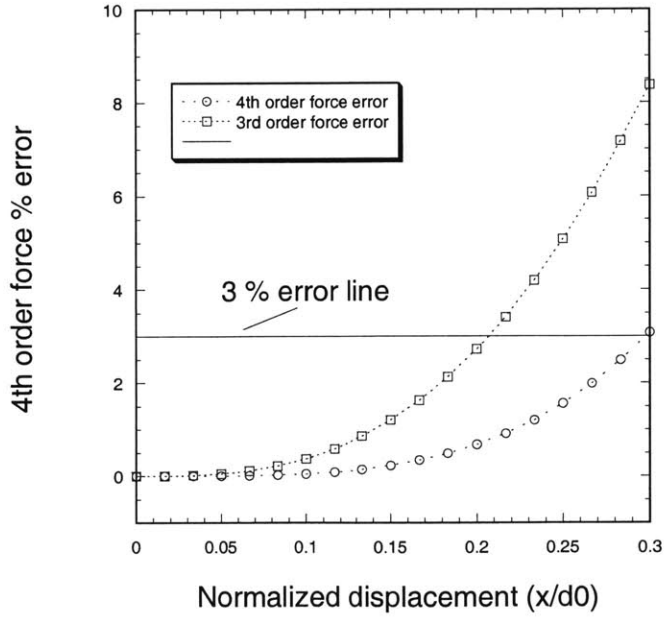

Figure 31 Error due to polynomial approximations for the force on a parallel plate capacitor.

A 3rd order multivariate polynomial is used as a default for fitting capacitance functions and is sufficient to capture the non-linear capacitance accurately for the examples we present in the following sections. Our implementation does, however, allow a designer to specify any order for the multivariate polynomial, or a rational polynomial, when the default setting is insufficient. We note here that the convergence of the Levenberg-Marquardt algorithm became unreliable for fits of multivariate polynomials above 4th order. A singular value decomposition based routine [38] was effective in these cases.

One issue of great significance that is not addressed in this thesis is the rapid growth in the number of coefficients required in our multivariate polynomials, or rational polynomials, as the polynomial order or number of modes increases. The general form for the multivariate polynomial is

$$U_d = \sum_{i_1=0}^{R_1} \cdots \sum_{i_m=0}^{R_m} a_{i_1 \cdots i_m} q_1^{i_1} \cdots q_m^{i_m} \tag{60}$$

and the number of coefficients in this polynomial, n_c is given by

$$n_c = (R_1 + 1)(R_2 + 1) \cdots (R_m + 1) \tag{61}$$

Table 4 illustrates the growth in n_c quite clearly. Over three thousand terms are required for a fourth order multivariate polynomial with five modes. Assuming that the number of sample simulations required to fit this polynomial grows at the same rate, the computation time to perform these samples becomes impractical. For example, it is not unusual for a single capacitance computation to take over a minute to perform. If one simulation is performed per coefficient, the total computation time will be over fifty hours for a forth order polynomial with five modes.

Number of modes	3rd order polynomial (n_c)	4th order polynomial (n_c)
2	16	25
3	64	125
5	1024	3125

Table 4 Growth in the number of polynomial coefficients as the polynomial order and number of modes increases.

Although for many of the MEMS problems of interest we find that polynomials with fewer than two hundred coefficients is sufficient for an accurate model, it is imperative to find ways to reduce the rate of growth in computation time to make our modeling process more generally applicable.

For simplicity, if $R_1 = R_2 = \cdots R_m = R$, n_c grows as R^m. It is the cross-terms in the multivariate polynomial that lead to this exponential increase. Are all these cross-terms necessary to capture the potential energy accurately? This is certainly dependent on the non-linearity of a particular energy domain. For example, only terms of the form q_i^n, $q_i q_j$, and $q_i q_j^2$ (i and j are numbers from 1 to m, and n is any power from 0 to R_i) are required to accurately capture the elastostatic energy of the asymmetric plate example in section 4.8. For such a pared down (reduced) multivariate polynomial, the number of terms is given by

$$n_c = 1 + mR + \frac{m}{2}(m-1) + m(m-1) \tag{62}$$

This grows linearly with the polynomial order, and as $O(m^2)$ in the number of modes – much slower growth than the full polynomial. For a fourth order reduced multivariate polynomial with five modes, only 51 terms are required as compared to 3125 terms of the full multivariate polynomial. Mehner [19] also recognizes that the particular non-linearity exhibited by stress-stiffening does not require a full multivariate polynomial and implements a polynomial based representation requiring fewer terms.

Finally, it may also be possible to construct models requiring less computation time by reducing the "volume" of mode space that must be captured by the model. Even in a state space spanned by a reduced set of modes, the observable trajectories of a particular system might lie within a tightly confined region within this space (see Figure 32). If this is true, and this subspace may be identified, models requiring less computation could be constructed. Rewienski et al. [41] propose a promising technique that identifies such a subspace and constructs a reduced-order model based on a piecewise-linear representation of this subspace.

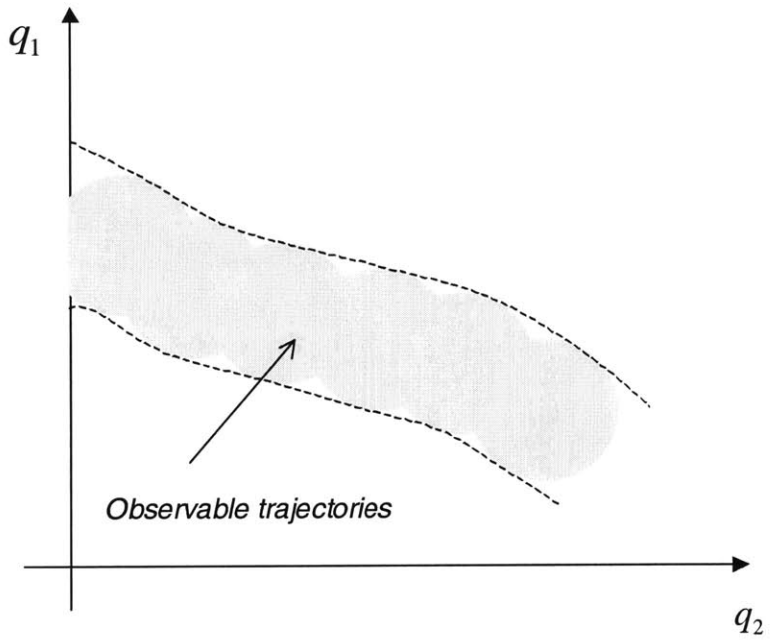

Figure 32 Observable trajectories in a two-dimensional state space.

5.5 Implementation

The modified CHURN process presented in this chapter is implemented in the MEMCAD [29] framework. Figure 33 is an outline of our software implementation. The clear boxes represent information that a user must provide through a graphical user interface (GUI). A user must provide the meshed description of a device, a model order (number of modes), and maximum operating amplitude of deflection. The software will then perform the remaining tasks automatically producing a SABER/MAST [34] macromodel file at the end. In the event that the automatic settings are insufficient, the user has the option of adjusting several model criteria. The user can select modes manually, select modal operating ranges, polynomial types for function fitting, and polynomial order. The majority of the code is written in the Glish [29] scripting language, with some modules written in C/C++.

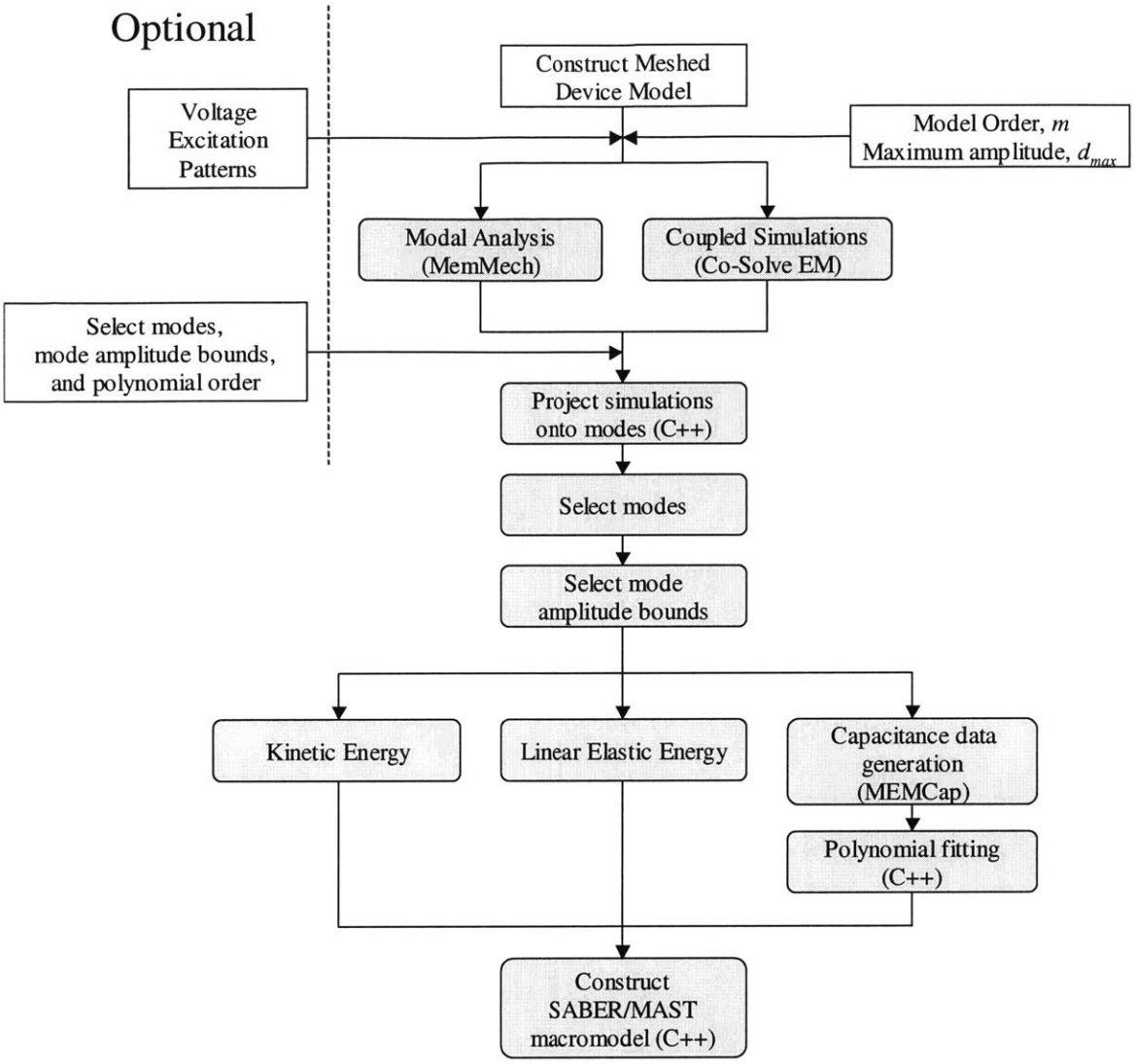

Figure 33 Overview of the implementation of the modified CHURN process.

5.6 High-frequency band-pass filter

The techniques presented in the previous sections are applied to a polysilicon high-Q HF band-pass filter [3]. The band-pass filter, shown in Figure 34, consists of two resonators formed by mechanical beams, coupled together by a crossbar (spring coupler). Without the crossbar the two resonators have identical resonant frequencies. The crossbar couples the two resonators and splits this degeneracy by creating a symmetric and an anti-symmetric mode. The distance from the anchors of the crossbar determines the frequency separation of these two modes and hence the bandwidth of this filter.

The filter is modeled with the mesh shown in Figure 35. There are two significant differences in geometry between the filter and the meshed representation. The mesh does not capture the conformal nature of the polysilicon layer, including non-ideal anchors that enhance the compliance of the structure. Instead, an effective resonator length is used to model the additional compliance. This simplifies the mesh, and also makes it possible to lump the effect of process variations on resonant frequency into this effective length. Bannon et al. [3] also point out that there are depletion effects in the non-degenerately-doped polysilicon layer. The effect of a depletion region is modeled using an effective gap height greater than the measured value of 1300A. The procedure in [3] of extracting these effective parameters from data on resonant frequency versus bias voltage for a simple single resonant beam test structure using an analytical model is followed. Measured values are used for all remaining dimensions. The measured and simulated device values are presented in Table 5.

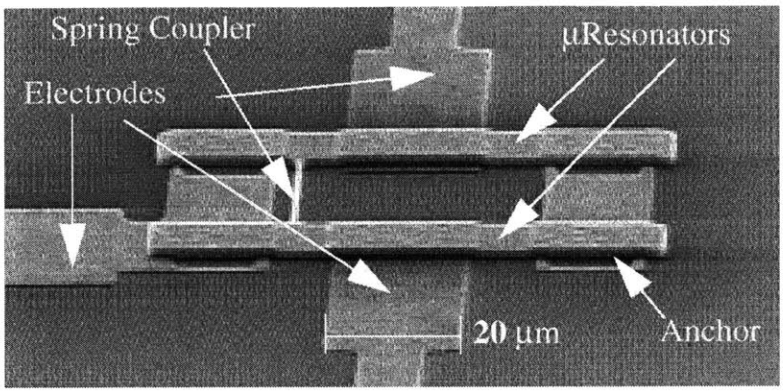

Figure 34 SEM photograph of a polysilicon high-Q HF resonator [3]. (SEM photograph courtesy of Clark T.-C. Nguyen)

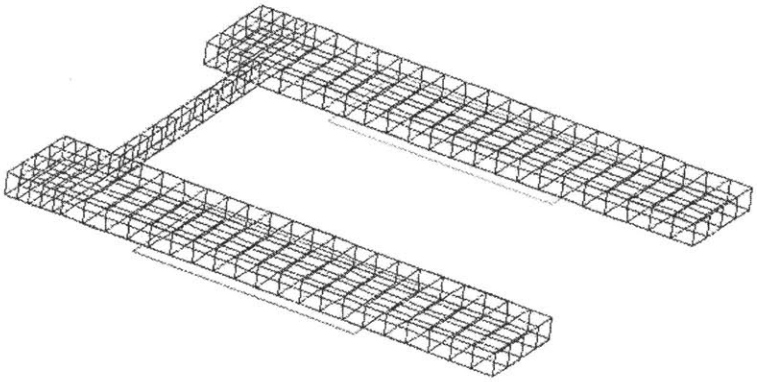

Figure 35 Mesh representation of the microelectromechanical resonator in Figure 34.

	Measured	Simulated
μRes Beam Length	40.8μm	43.532μm
μRes Beam Width	8μm	8μm
Structural layer thickness	1.9μm	1.9μm
Coupling beam location	4.08μm	4.48μm
Coupling beam length	20.35μm	20.35μm
Coupling beam width	0.75μm	0.75μm
Electrode to μRes gap	1300A	1985A
Electrode width	20μm	20μm
Young's modulus	150GPa	150GPa
Polysilicon density	2300kg/m^3	2300kg/m^3
Filter DC-bias	35V	35V

Table 5 Measured and simulated device values.

The macro-model is built using the automated multi-electrode CHURN process described in the previous sections with two modes, and maximum device motion amplitude of 300A. The simulated filter center frequency is within 0.5% of the experimentally measured value of 7.81MHz. It is not possible to improve on this accuracy using extracted parameters from a test structure, as there exist device-to-device variations [3]. Experimental data for the filter must be directly used to obtain a closer match. In practice, a second model is built with an effective length close to the first and the change in center frequency is found. Since these two data points are close together, a linear interpolation is used to obtain the correct effective length and center frequency for a final third model. Each model takes approximately three hours to build on a SUN Ultra 10 workstation with 1 GB of memory. The testing circuit used to obtain simulated frequency response curves is shown in Figure 36. Results from the simulations are shown in Figure 37. These system level simulations took just a few seconds to complete.

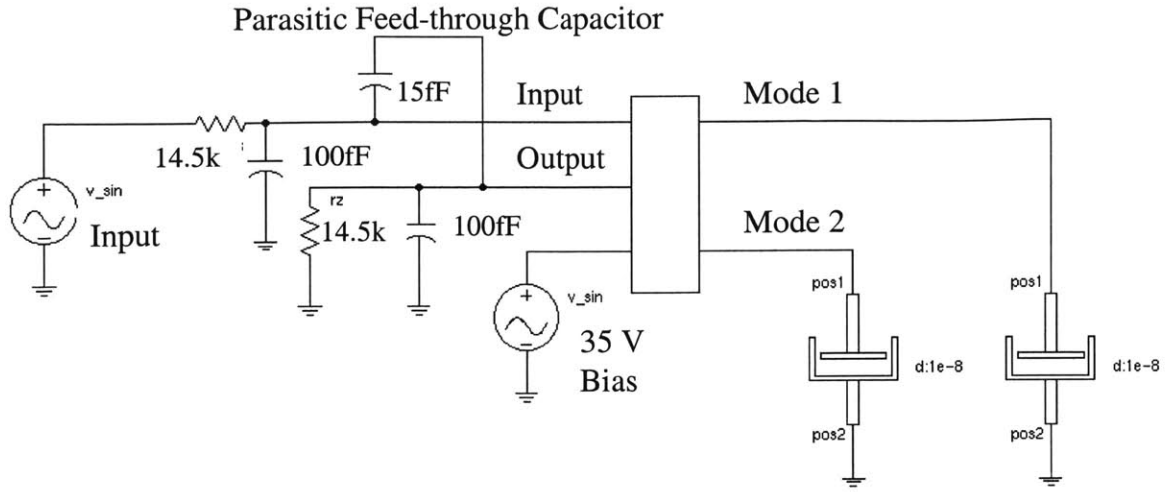

Figure 36 System level model of the HQ-filter testing circuit used to obtain the frequency response curves shown in Figure 37.

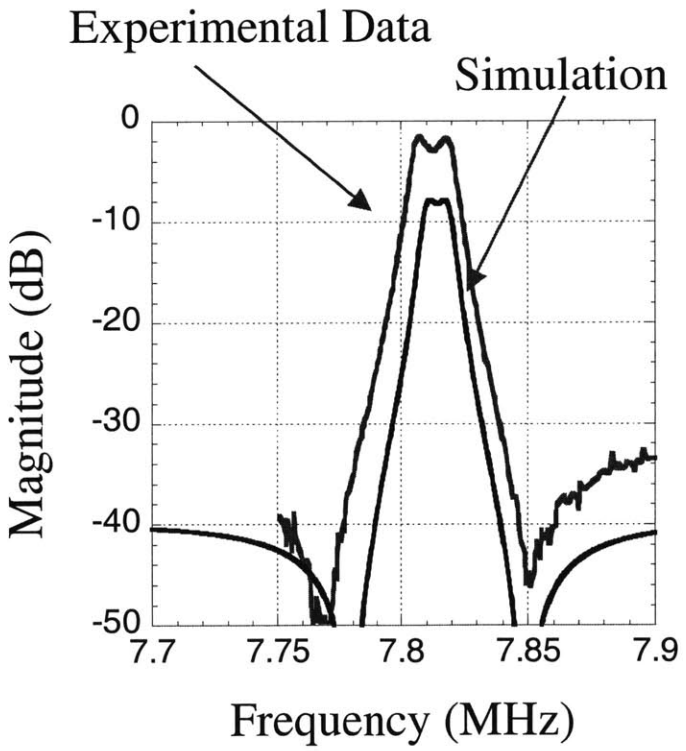

Figure 37 Simulated and measured curves for the frequency response for filter.

5.7 Complex filters

One significant advantage of our approach over hand-built models is the ability to extend it easily to more complex filter designs. As an example, we propose and model a three-resonator filter design (Figure 38). Frequency characteristics for the pass-band of this device are shown in *Figure 39*. Our model captures the non-linear, large-signal behavior of the device, including the important spring softening effect used to control the filter center frequency. This model required thirty minutes for a user to create a mesh, and approximately seven hours for the automatic model generation.

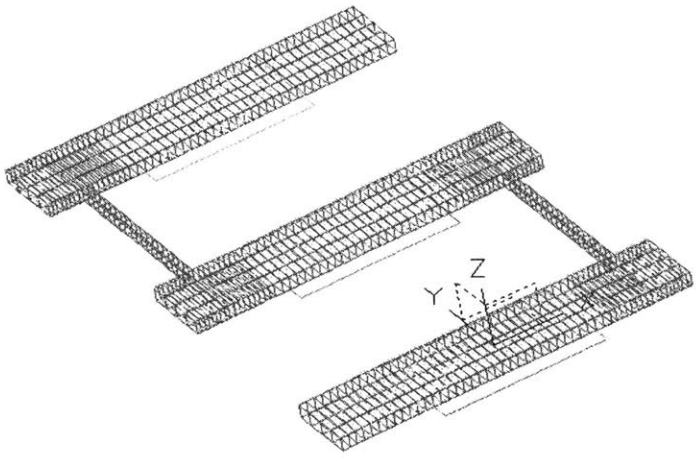

Figure 38 Mesh representation of a three-resonator filter design.

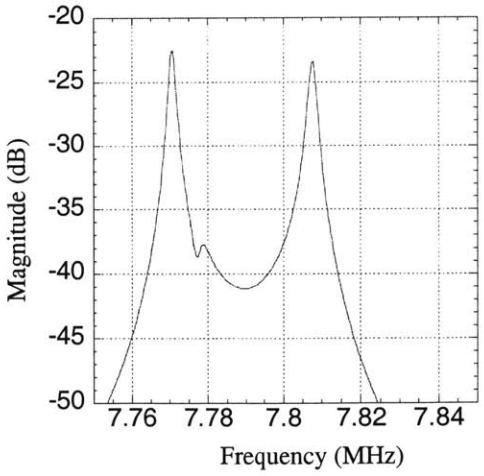

Figure 39 Simulated spectrum for the three-resonator filter. One can see the addition of a third peak within the pass-band for the filter. This filter was not optimized to minimize insertion loss or smooth out the pass-band.

5.8 Summary

This chapter discussed many of the issues involved in applying the CHURN process to practical situations in MEMS modeling. We first extended the CHURN process to model multi-electrode electrostatic devices that are more typical of the MEMS devices in use today. To this end, a general co-energy formulation was derived based on the capacitance matrix of a device. The electrostatic forces were then calculated from this co-energy.

Multiple electrodes also introduced several complexities in creating a reduced-order model that were not encountered with devices having two electrodes. The algorithm for selecting mode and mode amplitude bounds required multiple Co-Solve EM simulations, and a new selection criterion.

Heuristic algorithms were also introduced that automated the mode and mode amplitude selection. This reduced the degree of user involvement in the model construction process. For the automated case, a user (designer) was required to specify only the order of the model (number of modes), and maximum amplitude of deflection.

Additional work remains to be done on the selection and fitting of the multivariate polynomials used in our modified CHURN process. The growth in the number of terms in the polynomial was exponential and meant that the model construction time would become impractical when the number of modes, or polynomial order became large.

The modified CHURN process was implemented in the MEMCAD framework with a GUI for interaction with a designer. The models were written in the MAST language for insertion into the SABER system level simulator.

Finally, we constructed models of a fabricated high frequency microelectromechanical filter and compared simulation and experimental results. Some of the issues involved in modeling practical MEMS devices, such as approximating complex device geometry, were also discussed.

6 Summary and conclusions

This thesis explores techniques of constructing dynamic reduced-order models that enable the simulation of MEMS devices within the context of complete systems: sensors, actuators and electronics combined. We demonstrate these techniques on devices that employ non-linear electrostatic, magnetic and mechanical forces. We also explore the practical issues relating to the construction of our models including aspects of automating the model generation process. In addition, we compare experimental and simulation results from a fabricated microelectromechanical high frequency filter as a validation of our modeling methodology.

We adopt, in this thesis, a well-established modeling strategy of partitioning the physics of MEMS devices into conservative and non-conservative (dissipative) energy domains. We introduce effective techniques to capture conservative device behavior separately from a device's dissipative processes. These partitioned domains are then combined at the system level to form a complete description of a device. Our work builds upon the CHURN process, introduced by Gabbay, to model two independent electrode electromechanical devices exhibiting linear mechanical forces and non-linear electrostatic forces.

We demonstrate how CHURN is extensible to other physical domains using magnetic devices as an example in Chapter 3. We derive a magnetic co-energy formulation for Lorentz force and linear permeable material devices. The devices we model have inductances that are solely a function of mode amplitudes. However, there are many devices that do not fit this criterion, yet may be modeled using a co-energy formulation. Devices that exhibit magnetic flux saturation in the permeable material are a good illustration of this point. The inductance under saturation becomes a function not only of mode amplitudes, but also of the currents in the system. Devices that exhibit frequency dependent inductances or hysteretic behavior require alternative modeling strategies because the magnetic system is no longer conservative in nature. Thus, forces cannot be derived from a magnetic co-energy in these cases.

We then address the failure of the CHURN process to capture the geometrically non-linear effect of stress stiffening in Chapter 4. CHURN macromodels exhibit stiffness greater than the devices they model. The cause of this additional stiffness is established as the zero mode amplitude constraints on "higher-order" modes imposed by truncated modal superposition. These constraints prevent the device from relaxing naturally through Poisson contraction and therefore suppress the modal coupling essential to the device behavior. We show, using singular perturbation methods, that under certain conditions it is still possible to describe the device motion using a reduced set of "low-order" modes. The dynamics of the "higher-order" modes and the applied forces on these modes must be negligible. Under these conditions, we use a methodology that probes the mechanical behavior of the device using "low-order" modal forces to generate a strain energy function, while imposing zero modal force constraints on the "higher-order" modes. These force constraints allow relaxation in "higher-order" modes while still enabling model order reduction. Successful modeling results based on this force methodology are presented for a fixed-fixed beam and asymmetrically supported plate.

Finally, we explore heuristic techniques of automating the model construction process in Chapter 5. We show how modes and modal bounds may be selected automatically from a set of Co-Solve EM simulations for multi-electrode electromechanical devices. This leaves a designer to specify only the model order and maximum displacement at the start of the modeling process. We model a high frequency microelectromechanical filter and show favorable comparison of experimental and simulated results. This example also illustrates some of the issues encountered in modeling real MEMS devices where device geometry, dimensions, and physics must typically be approximated. Often, multiple iterations are made through the model generation process to account for, or explore the implications of these approximations. If the time required to generate these models is not relatively short (on the order of minutes or hours), our modeling techniques become impractical. Keeping this in mind, the exponential growth in the polynomial representations of energy in the CHURN process is a cause for significant concern. We have suggested domain specific methods of reducing the growth in model size, such as the elimination of cross-terms, but we have not presented a general strategy to overcome this problem. Perhaps an alternative representation to polynomials, such as a piece-wise

linear approximation around a trajectory as suggested by Rewienski will provide a successful solution.

One significant issue that remains to be addressed is the incorporation of dissipative mechanisms, such as damping, into our modeling process. We introduce damping elements at the system level that interact with our conservative model through the device's mechanical ports. We may generate these damping models separately using any technique appropriate for a particular dissipative mechanism. These mechanisms vary considerably in their complexity. Damping in resonant devices operated in vacuum, for example, can often be captured through linear dashpots for each mode. On the other hand, compressible squeeze film damping (CSQFD) exhibits high non-linearity for large amplitude motion[51][52]. Unlike the conservative processes we encountered in this thesis, CSQFD is dependent on both the mode amplitudes and mode velocities. Constructing a model by sampling the doubled state-space spanned by these variables as we do in the CHURN process quickly becomes impractical. Several successful approaches at building damping models depend on time series data from a few dynamic finite element simulations (FEM)[12][41]. Fully coupled FEM simulations are slow, but it may be possible to speed up these simulations by replacing part of the FEM with a fast CHURN based model of the conservative physics of a device. The CHURN model will then couple with a FEM representation of only the CSQFD. In the future, fast techniques of generating reduced-order models of dissipative processes must be developed to complement the models generated by the CHURN process.

The techniques we present in this thesis have demonstrated significant success in modeling various types of MEMS devices, including those that employ electrostatic, magnetic and non-linear mechanical forces for actuation and sensing. We implement tools that automate the construction of macromodels and verify our modeling methodology through comparison with experimental results. Our approach, along with other reduced-order modeling methodologies, bring the vision of accurately modeling entire microsystems – sensors, actuators and electronics -- on a computer workstation, a step closer to reality.

7 References

[1] ADXL50 Accelerometer Data Sheet, Analog Devices, Inc., One Technology Way, P.O. Box 9106, Norwood, MA 02062-9106, 1996.

[2] F. Ayazi, K. Najafi, "Design and Fabrication of a High-Performance Polysilicon Vibrating Ring Gyroscope," Eleventh IEEE/ASME International Workshop on Microelectromechanical Systems, Heidelberg, Germany, Jan. 25029, 1998.

[3] F.D. Bannon III, J.R. Clark, C.T..-C Nguyen, "High Q HF Microelectromechanical Filters," IEEE Journal of Solid-State Circuits, Vol. 35, No. 4, pp512-526, April 2000.

[4] OMM, Corporate HQ, 9410 Carroll Park Dr., San Diego, CA 92121.

[5] Analog Devices, Corporate Headquarters, One Technology Way, P. O. Box 9106, Norwood, MA 02062-9106.

[6] Lucent Technologies, Corporate Headquarters, 600 Mountain Avenue, Murray Hill, NJ 07974.

[7] SABER, Analogy Inc., Beaverton, OR 97008, http://www.analogy.com

[8] SPICE3 Users manual, EECS Dept., UC Berkeley, http://bwrc.eecs.berkeley.edu/Classes/IcBook/SPICE/

[9] H. Goldstein, Classical Mechanics, 2 nd edition, Addison-Wesley Publishing Company, pp. 16-21, 1981.

[10] G.K. Fedder, Q. Jing, "NODAS 1.3 – Nodal Design of Actuators and Sensors," IEEE/VIUF Int. Workshop on Behavioral Modeling and Simulation, Orlando, FL, Oct. 27-28, 1998.

[11] Y. Chen, J. White, "A Quadratic Method for Nonlinear Model Order Reduction," International Conference on Modeling and Simulation of Microsystems, Semiconductors, Sensors and Actuators, 2000.

[12] E. Hung, Y. Yang, S.D. Senturia, "Low-Order Models for Fast Dynamical Simulation of MEMS Microstructures," IEEE International Conference on Solid State Sensors and Actuators (Transducers '97), Vol. 2, pp. 1101-1104, 1997.

[13] M. Varghese, V. Rabinovich, S.D. Senturia, "Reduced-order modeling of Lorentz force actuation with mode shapes," International Conference on Modeling and Simulation of Microsystems, Semiconductors, Sensors and Actuators, San Juan, Puerto Rico, April, 1999.

[14] M. Varghese, V. Rabinovich, S.D. Senturia, "Reduced-order models of stress-stiffened MEMS structures," International Conference on Modeling and Simulation of Microsystems, Semiconductors, Sensors and Actuators, San Diego, April, 2000.

[15] M. Varghese, S.D. Senturia, J.R. Gilbert, V. Rabinovich, "Automatic Reduced-order Modeling in MEMCAD using Modal Basis Functions," Transducers '01, Munich, June, 2001.

[16] S.S. Rao, "Mechanical Vibrations," 3rd edition, Addison-Wesley Publishing Company, 1995.

[17] S.D. Senturia, "CAD challenges for microsensors, microactuators, and Microsystems," Proc. IEEE, vol. 86, no. 8, , pp. 1611-26, Aug. 1998.

[18] L.D. Gabbay, J.E. Mehner, and S.D. Senturia, "Computer-Aided Generation of Nonlinear reduced-Order Dynamic Macromodels: I. Non-Stress-Stiffened Case," J. Microelectromechanical Systems, Vol.9, No. 2, , pp262-9,2000.

[19] J.E. Mehner, L.D. Gabbay, and S.D. Senturia, "Computer-Aided Generation of Nonlinear Reduced-Order Dynamic Macromodels: II Stress-Stiffened Case," J. Microelectromechanical Systems, Vol. 9, No. 2, 2000.

[20] G.K. Anathasuresh, R. K. Gupta, and Stephen D. Senturia, " An Approach to macromodeling of MEMS for Nonlinear Dynamic Simulation," DSC-Vol. 59, Microelectromechanical Systmes, ASME 1996, pp. 401-407.

[21] D. Wickenden, T. Kistenmacher, R. Osiander, S. Ecelberger, R. Givens, J. Murphy, "Development of Miniature Magnetometers," Johns Hopkins APL Technical Digest, Vol. 18, No. 2, pp. 271-278, 1997.

[22] B. Shen, W. Allegretto, Y. Ma, B. Yu, M. Hu, and A. Robinson, "Cantilever Micromachined Structures in CMOS Technology with Magnetic Actuation," Sensors and Materials, Vol. 9, No. 6, pp 347-362, 1997.

[23] A. Harris, J Burdess, D. Wood, R. Langford, G. Williams, M. Ward, M. McNie, "Issues associated with the design, fabrication and testing of crystalline silicon ring gyroscope with electromagnetic actuation and sensing," J. Micromech. Microeng., No 8, pp284-292, 1998.

[24] S. Martin, M. Butler, J. Spates, M. Mitchell, W. Schubert, "Flexural plate wave resonator excited with Lorentz forces," Journal of Applied Physics, Vol. 83, No. 9, 1998.

[25] W. P. Taylor, M. G. Allen, C. R. Dauwalter, "A Fully Integrated Magnetically Actuated Micromachined Relay," Proceedings 1996 Solid State Sensor and Actuator Workshop, Hilton Head, pp.231-234, 1996.

[26] AMPERES, Users and Technical Manual, Integrated Engineering Software, 300 Cree Crescent, Winnipeg, Manitoba, R3J 3W9, Canada.

[27] ANSYS 5.4, Ansys, Inc., Southpointe, 275 Technology Drive, Canonsburg, PA 15317, 1998.

[28] L. Gabbay, "Computer Aided Macromodeling for MEMS," Ph.D. Thesis, Department of Electrical Engineering, Massachusetts Institute of Technology, Cambridge, MA, 1998.

[29] MEMCAD 5 Manual, Coventor Inc., 5511 Capital Center Dr., Raleigh, NC, 1999.

[30] Prof. Jacob White, EECS, MIT, personal communication.

[31] H. Haus, J. Melcher, "Electromagnetic Fields and Energy," Pretence Hall, 1989.

[32] MATLAB, The MathWorks Inc., Natick, MA 01760, http://www.mathworks.com

[33] R.K. Gupta, E. Hung, Y.-J. Yang, G.K. Ananthasuresh, S.D. Senturia, "Pull-in Dynamics of Electrostatically-Actuated Beams," Late News Poster Session Supplemental Digest at Solid-State Sensor and Actuator Workshop, Hilton Head, SC, 1996.

[34] MAST Reference Manual, Analogy Inc., 19205 SW Gemini Drive, Beaverton, OR 97008.

[35] E. Christen, K. Bakalar, "VHDL-AMS – A Hardware Description Lanugage for Analog and Miced-Signal Applications," IEEE Transactions on Circuits and Systems – II: Analog and Digital Signal Processing, Vol. 46, No. 10, October 1999.

[36] W.H. Press, W.T. Vetterling, S.A. Teukolsky, B.P. Flannery, "Numerical recipes in C: The Art of Scientific Computing," 2nd ed. Cambridge University Press, pp676-681, 1995.

[37] S.P. Timoshenko, J.N. Goodier, "Theory of Elasticity," Third Edition, McGraw Hill.

[38] C.S. Lee, S. Han and N.C. MacDonald, "Multiple Depth, Single Crystal Silicon Microactuators for Large Displacements Fabricated by Deep Reactive Ion Etching," Solid-State Sensor and Actuator Workshop, Hilton Head Island, pp. 35-50, 1998.

[39] W.H. Press, S. A. Teukolsky, W.T. Vetterling, B.P. Flannery, "Numerical recipies in C, The Art of Scientific Computing," Second Edition, Cambridge University Press, 1992.

[40] H. Goldstein, "Classical Mechanics," 2 nd edition, Addison-Wesley Publishing Company, pp. 16-21, 1981.

[41] M. Rewienski, J. White, "A Trajectory Piecewise-Linear Approach to Model Order Reduction and Fast Simulation of Nonlinear Circuits and Micromachined Devices," The International Conference on Computer Aided Design (ICCAD) 2001, SanJose, CA, Nov. 4-8 2001

[42] T. Mukherjee, G.K. Fedder, D. Ramaswamy, J. White, "Emerging Simulation Approaches for Micromachined Devices," IEEE Transactions on Computer-Aided Design of Integrated Circuits and Systems, Vol. 19, No. 12, December 2000.

[43] Y.C. Liang, W.Z. Lin, H.P. Lee, S.P. Lim, K.H. Lee, D.P. Feng, "A neural-network-based method of model reduction for the dynamic simulation of MEMS," Journal of Micromechanics and Microengineering, Vol. 11, pp. 226-233, 2001.

[44] W. Weaver, Jr., S.P. Timoshenko, D.H. Young, "Vibration Problems in Engineering," 5th edition, Wiley Interscience, 1990.

[45] M. Varghese, R. Amantea, D. Sauer, S. D. Senturia, "Resistive Damping of Pulse-Sensed Capacitive Position Sensors," Proceedings of Transducers' 97, Volume 2, pp. 1121-1124, Chicago, June 16-19, 1997.

[46] R. K. Gupta, S.D. Senturia, "Pull-in Time Dynamics as a Measure of Absolute Pressure," MEMS '97, pp.290-293, Nagoya, Japan, January 26-30, 1997.

[47] H. A.C. Tilmans, "Equivalent Circuit Representation of Electromechanical Transducers: I. Lumped-parameter systems [micromechanical systems}," J. Micromechanics and Microengineering, vol. 6, no. 1, pp 157-176, 1996.

[48] C. Lu, M. Lemkin, B. E. Boser, "A monolithic surface micromachined accelerometer with digital output," IEEE Int. Solid-State Conference, San Francisco, CA, Feb. 1995.

[49] G. K. Fedder, Q. Jing, "NODAS 1.3 – Nodal Design of Actuators and Sensors," BMAS '98, IEEE/VIUF International Workshop on Behavioral Modeling and Simulation, Orlando, FL, October 27-28, 1998.

[50] D.S. Naidu, "Singular perturbation methodology in control systems," Peter Peregrinus Ltd., United Kingdom, 1998.

[51] Y.-J. Yang, M.A. Gretillat, S.D. Senturia, "Effect of air damping on the dynamics of nonuniform deformations of microstructures," Transducers '97, pp. 1093-1096.

[52] Y.-J. Yang, S.D. Senturia, "Numerical simulation of compressible squeeze-film damping," Proc. Solid State Sensor and Actuator Workshop, Hilton Head, SC, 1996, pp. 76-79.

Appendix A Multi-port force formulations

A.1. Magnetic co-energy formulation

We derive here the magnetic co-energy formulation for calculating forces for a general Lorentz force device modeled with n electrical ports and m mechanical modes (see Figure 40). The ports govern the energy flowing in and out of the device, and the rate of change in potential energy of the device is

$$\frac{dU_{magnetostatic}}{dt} = \sum_{j=1}^{n} i_j v_j + \sum_{k=1}^{m} f_k \frac{dq_k}{dt} \tag{63}$$

Multiplying through by dt, and substituing $v_j = \frac{d\lambda_j}{dt}$, equation (63) becomes

$$dU_{magnetostatic} = \sum_{j=1}^{n} i_j d\lambda_j + \sum_{k=1}^{m} f_k dq_k \tag{64}$$

We now define the magnetic co-energy as

$$U^*_{magnetostatic} = \sum_{j=1}^{n} i_j \lambda_j - w_m \tag{65}$$

and use the following identity

$$d(\sum_{j=1}^{n} i_j \lambda_j) = \sum_{j=1}^{n} i_j d\lambda_j + \sum_{j=1}^{n} \lambda_j di_j \tag{66}$$

to recast equation (64) as

$$dU^*_{magnetostatic} = \sum_{j=1}^{n} \lambda_j di_j - \sum_{k=1}^{m} f_k dq_k \tag{67}$$

Now, the change $dU^*_{magnetostatic}$ is also given by

$$dU^*_{magnetostatic} = \sum_{j=1}^{n} \frac{\partial U^*_{magnetostatic}}{\partial i_j} di_j + \sum_{k=1}^{m} \frac{\partial U^*_{magnetostatic}}{\partial q_k} dq_k \tag{68}$$

In order for equation (67) and equation (68) to be consistent, the flux linkages and force must equal:

$$\lambda_j = \frac{\partial U^*_{magnetostatic}}{\partial i_j} \tag{69}$$

$$f_k = -\frac{\partial U^*_{magnetostatic}}{\partial q_k} \tag{70}$$

Equation (70) is a convenient way to calculate the generalized force f_k if the magnetic co-energy is known. Thus, it remains to find the co-energy. One means of doing this is by integrating equation (67)

$$U^*_{magnetostatic} = \int \left(\sum_{j=1}^{n} \lambda_j di_j - \sum_{k=1}^{m} f_k dq_k \right) \tag{71}$$

Since the system is conservative, the co-energy is independent of the integration path. Therefore, consider integrating the terms $f_k dq_k$ first, with all currents in the system set to zero. The force f_k is zero in the absence of currents, so the contribution of the integral $\int \sum_{k=1}^{m} f_k dq_k$ is also zero.

The next step is to integrate the terms $\lambda_j di_j$. To perform this integral it is convenient to express the flux linkages λ_j in terms of the currents i_j using the inductance matrix $[L]$ associated with the system

$$\begin{bmatrix} \lambda_1 \\ \vdots \\ \lambda_n \end{bmatrix} = \begin{bmatrix} L_{11} & \cdots & L_{1n} \\ \vdots & \ddots & \vdots \\ L_{n1} & \cdots & L_{nn} \end{bmatrix} \begin{bmatrix} i_1 \\ \vdots \\ i_n \end{bmatrix} \tag{72}$$

Each of the inductance entries is a function of the positional state, $\vec{q}$. Keeping in mind that equation (71) is a path integral, the magnetic co-energy now evaluates to

$$U^*_{magnetostatic} = \sum_{r=1}^{n}\sum_{s=1}^{n}\frac{1}{2}L_{rs}i_r i_s \tag{73}$$

One possible path is to move along each current "axis" sequentially, increasing i_1 to its final value, then i_2 and so on up to i_n. Using this form of the co-energy, the force f_k in equation (38) becomes

$$f_k = -\sum_{r=1}^{n}\sum_{s=1}^{n}\frac{1}{2}\frac{\partial L_{rs}}{\partial q_k}i_r i_s \tag{74}$$

The problem of finding an analytical representation for the force f_k reduces to finding an analytical form for the inductances $L_{rs}(q_1,\cdots,q_m)$.

A.2. Electrostatic co-energy

The generalized electrostatic forces have a very similar derivation. We only state the final results here for reference:

$$U^*_{magnetostatic} = \sum_{r=1}^{n}\sum_{s=1}^{n}\frac{1}{2}C_{rs}V_r V_s$$

and

$$f_k = -\sum_{r=1}^{n}\sum_{s=1}^{n}\frac{1}{2}\frac{\partial C_{rs}}{\partial q_k}V_r V_s$$

where C_{rs} are the entries in the capacitance matrix of the system.

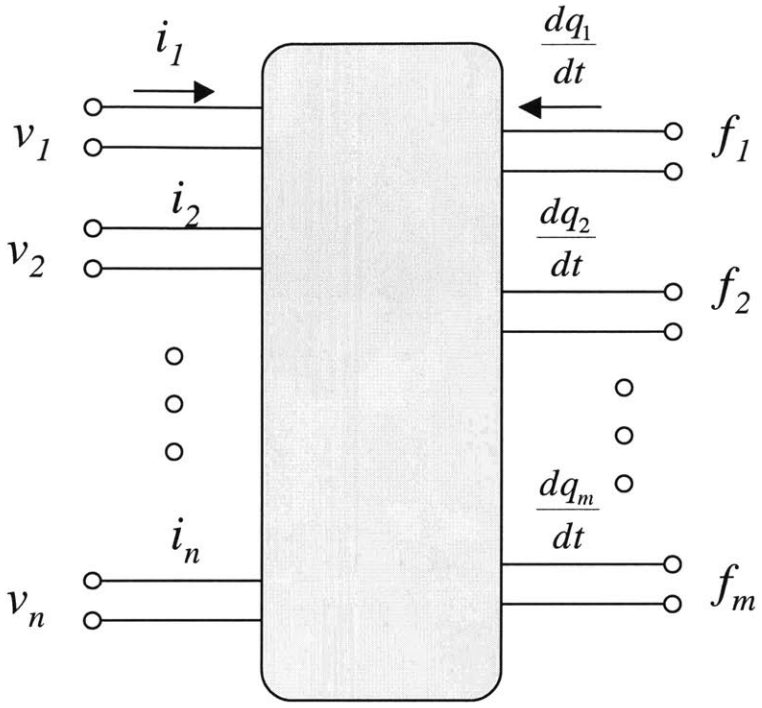

Figure 40 Network representation of a Lorentz force device with n electrical ports, and modeled with m mechanical ports.

Appendix B Modal force constraints

In Chapter 4 we demonstrated a methodology for calculating an accurate strain energy function using modal forces. We show here that modal forces do not directly constrain the motion of the higher order modes and thus allow the relaxation necessary to capture an accurate strain energy function.

The force on the mechanical system in the modal force methodology (Figure 20) is

$$\vec{F} = \vec{F}_{eqm} + \sum_{i=1}^{m} \frac{f_i}{k_i} \vec{F}_i \tag{75}$$

The modal force vectors, $\vec{F}_i$, are derived from the mode shapes, $\vec{\varphi}_i$, through the linear stiffness matrix, $[K]_{NxN}$.

$$\vec{F}_i = [K]_{NxN} \vec{\varphi}_i \tag{76}$$

When the modal forces $\{f_1, \cdots f_m\}$ are applied to the mechanical system, it settles into its equilibrium state $\{q_1, \cdots q_m\}$. For small excursions away from this equilibrium state in a particular mode q_i, where $i \le m$, the system must do work against the corresponding modal force:

$$\Delta U_{mechanical} = \left(\Delta q_i \vec{\varphi}_i^T\right)\left(\frac{f_i}{k_i}\vec{F}_i\right) = \left(\Delta q_i \frac{f_i}{k_i}\right)\left(\vec{\varphi}_i^T [K]_{NxN} \varphi_i\right) = \Delta q_i f_i \tag{77}$$

However, for small excursions in mode q_i, where $i > m$, the system does no work against the modal forces $\{f_1, \cdots f_m\}$.

$$\Delta U_{mechanical} = \left(\Delta q_i \vec{\varphi}_i^T\right)\left(\frac{f_j}{k_j}\vec{F}_j\right) = \left(\Delta q_i \frac{f_j}{k_j}\right)\left(\vec{\varphi}_i^T [K]_{NxN} \varphi_j\right) = 0 \tag{78}$$

because the mode shapes $\vec{\varphi}_i$ are orthogonal over the stiffness matrix and $i \neq j$. This means that the mechanical system is unconstrained by the modal forces, and hence relaxed in the higher order modes.

Appendix C Modal coupling to higher-order modes

In this appendix we demonstrate how modal coupling between lower and higher order modes lead to errors in the CHURN process. In addition we show that it is possible to describe such a system using only low order modes if certain important conditions are satisfied.

Here we use the terms "low order" and "high order" modes loosely. Low and high do not refer to the frequency order of the modes. Low order modes specifically refer to the modes that are selected for use in the macromodel, and high order modes are the remaining modes of the system. For a mesh with N degrees of freedom, there are m low order modes, $\vec{q}_{low}$, and (N-m) high order modes, $\vec{q}_{high}$.

The equation of motion in modal coordinates for the system as a whole is given by

$$[m_G]_{NxN} \frac{d^2}{dt^2} \vec{q}^{Nx1} = -[k_{linearized}]_{NxN} \vec{q}^{Nx1} + f_e^{Nx1} \tag{79}$$

where $[m_G]$ is the N by N diagonal generalized modal mass matrix, $\vec{q}$ is the vector of modal amplitudes, $[k_{linearized}]$ is the linearized modal stiffness matrix about operating point $\vec{q}$, and $\vec{f}_e$ is the vector of electrostatic forces acting on the modes. This equation may be re-written to highlight the low and high order mode contributions.

$$\begin{array}{c} \overset{m}{\longleftrightarrow} \quad \overset{N-m}{\longleftrightarrow} \\ \begin{matrix} m \\ \updownarrow \\ N-m \\ \updownarrow \end{matrix} \begin{bmatrix} m_{low} & 0 \\ 0 & m_{high} \end{bmatrix} \end{array} \begin{bmatrix} \frac{d^2}{dt^2}\vec{q}_{low} \\ \frac{d^2}{dt^2}\vec{q}_{high} \end{bmatrix} = - \begin{bmatrix} k_{low-low} & k_{low-high} \\ k_{high-low} & k_{high-high} \end{bmatrix} \begin{bmatrix} \vec{q}_{low} \\ \vec{q}_{high} \end{bmatrix} + \begin{bmatrix} \vec{f}_{low} \\ \vec{f}_{high} \end{bmatrix} \tag{80}$$

where the mass matix, $[m_G]$, is composed of two submatrices, $[m_{low}]$, and $[m_{high}]$, the modal amplitudes are expressed in terms of the low and high order mode amplitudes, $\vec{q}_{low}$, and $\vec{q}_{high}$, respectively. The stiffness matrix is composed of four submatrices: $[k_{low-low}]$ captures the stiffness and interaction of the low order modes, $[k_{high-high}]$ captures the stiffness and interaction of the high order modes, $[k_{low-high}]$, and $[k_{high-low}]$ capture the coupling between low and high order modes. Finally, the electrostatic force, $\vec{f}_e$, is composed of the forces acting on the low and high order modes, $\vec{f}_{low}$, and $\vec{f}_{high}$.

Under the conditions that the dynamics of the higher order modes, $\frac{d^2}{dt^2}\vec{q}_{high}$, and the electrostatic forces acting on these modes, $\vec{f}_{high}$, are negligible, we can simplify equation (80) significantly using the techniques of singular perturbation methods [50].

$$\begin{array}{c} \\ m \\ N-m \end{array}\begin{array}{c} \begin{array}{cc} m & N-m \end{array} \\ \begin{bmatrix} m_{low} & 0 \\ 0 & m_{high} \end{bmatrix} \end{array}\begin{bmatrix} \frac{d^2}{dt^2}\vec{q}_{low} \\ \frac{d^2}{dt^2}\vec{q}_{high} \approx 0 \end{bmatrix} = -\begin{bmatrix} k_{low-low} & k_{low-high} \\ k_{high-low} & k_{high-high} \end{bmatrix}\begin{bmatrix} \vec{q}_{low} \\ \vec{q}_{high} \end{bmatrix} + \begin{bmatrix} \vec{f}_{low} \\ \vec{f}_{high} \approx 0 \end{bmatrix}$$

(81)

The first m rows of equation (81) describe the dynamics of the low order modes

$$[m_{low}]\frac{d^2}{dt^2}\vec{q}_{low} = -[m_{low-low}]\vec{q}_{low} - [k_{low-high}]\vec{q}_{high} + \vec{f}_{low} \tag{82}$$

while the remaining (N-m) rows describe the coupling between low and high order modes

$$0 = -[k_{high-low}]\vec{q}_{low} - [k_{high-high}]\vec{q}_{high} \tag{83}$$

The above equation may be solved to express the high order mode amplitudes in terms of low order mode amplitudes.

(84) $$\vec{q}_{high} = -[k_{high-high}]^{-1}[k_{high-low}]\vec{q}_{low}$$

Thus, $\vec{q}_{high}$ is given by the product of the compliance of the high order modes, $[k_{high-high}]^{-1}$, the coupling between high and low order modes, $[k_{high-low}]$, and the amplitude of the low order modes, $\vec{q}_{low}$. We can use the result in equation (84) to express equation (82) solely in terms of the low order modes.

(85) $$[m_{low}]\frac{d^2}{dt^2}\vec{q}_{low} = \left(-[k_{low-low}] + [k_{low-high}][k_{high-high}]^{-1}[k_{high-low}]\right)\vec{q}_{low} + \vec{f}_{low}$$

Equation (85) shows that even when the coupling between low and high order modes is significant, the state of the system may be described by only the set of low order modes. Any reduced order model must however capture the modal coupling represented here by the term $[k_{low-high}][k_{high-high}]^{-1}[k_{high-low}]$. The CHURN process fails to capture this coupling because it explicitly suppresses the higher order modes, therefore violating equation (84).

In Chapter 4 we utilize an alternative approach to capturing the modal coupling to higher order modes. Consider equation (85) in its static limit when $\frac{d^2}{dt^2}\vec{q}_{low} = 0$.

(86) $$\left([k_{low-low}] - [k_{low-high}][k_{high-high}]^{-1}[k_{high-low}]\right)\vec{q}_{low} = \vec{f}_{low}$$

Our intent is to capture the relationship between the applied forces and the modal amplitudes. We do this by applying forces, $\vec{f}_{low}$, and measuring the mechanical response, $\vec{q}_{low}$, to determine the term $[k_{low-low}] - [k_{low-high}][k_{high-high}]^{-1}[k_{high-low}]$. In practice, however, we cannot do this directly in modal co-ordinates because our mechanical solvers operate in the finite element "nodal" co-ordinate system. They solve the following equation:

(87) $$[K_{linearized}]_{NxN}\,\vec{y} = \vec{F}_{Nx1}$$

where $\vec{y}$ is the position vector in Chapter 2, $[K_{linearized}]_{NxN}$ is the linearized "nodal" stiffness matrix about operating point $\vec{y}$, and $\vec{F}_{Nx1}$ is an applied nodal force vector. We apply a superposition of modal forces as a load on the mechanical system

$$\vec{F}_{Nx1} = \sum_{i=1}^{m} \frac{f_i}{k_i} \vec{F}_i \tag{88}$$

where k_i is a modal stiffness and $\vec{F}_i$ is a modal force given by $[K]_{NxN} \vec{\varphi}_i$ (see Chapter 4). Equation (87) is then solved for the mechanical response, $\vec{y}$. Following this, we project $\vec{y}$ onto the modes to obtain the response in modal co-ordinates.

$$q_i = \frac{(\vec{y} - \vec{y}_{eqm})^T [M]_{NxN} \vec{\varphi}_i}{\varphi_i^T [M]_{NxN} \vec{\varphi}_i} \tag{89}$$

$[M]_{NxN}$ is the "nodal" mass matrix. This solution is identical to that obtained by solving equation (79) under static conditions and hence by extension equation (86). We show this by pre-multiplying equation (87) by the transpose of the modal matrix , $[P]^T_{NxN}$.

$$[P]^T_{NxN} [K_{linearized}]_{NxN} [P]_{NxN} \vec{q}^{Nx1} = [P]^T \sum_{i=1}^{m} \frac{f_i}{k_i} \vec{F} = [P]^T_{NxN} \sum_{i=1}^{m} \frac{f_i}{k_i} [K]_{NxN} \varphi_i = \vec{f}_{low} \tag{90}$$

The above equation reduces to

$$[k_{linearized}]_{NxN} \vec{q}^{Nx1} = \vec{f}_{low} \tag{91}$$

which is equation (79). Again, this in turn may be transformed into equation (86) as we have shown earlier. Since we are interested in the relationship between the low-order modes and the applied forces, we only have to calculate the projection of $\vec{y}$ onto these modes using equation (89).